



Radiation and Polarization Signatures from Magnetic Reconnection in Relativistic Jets. I. A Systematic Study

Haocheng Zhang¹ , Xiaocan Li² , Dimitrios Giannios¹ , Fan Guo³ , Yi-Hsin Liu² , and Lingyi Dong¹

¹ Department of Physics and Astronomy, Purdue University, West Lafayette, IN 47907, USA; astrophyshc@hotmail.com

² Dartmouth College, Hanover, NH 03750, USA

³ Theoretical Division, Los Alamos National Lab, Los Alamos, NM 87545, USA

Received 2020 January 30; revised 2020 August 19; accepted 2020 August 21; published 2020 October 5

Abstract

Blazars are relativistic magnetized plasma outflows from supermassive black holes that point very close to our line of sight. Their emission is nonthermal-dominated and highly variable across the entire electromagnetic spectrum. Relativistic magnetic reconnection has been proposed as the driver of particle acceleration during blazar flares. While recent particle-in-cell (PIC) simulations have self-consistently studied the evolution of magnetic reconnection and particle acceleration therein, the resulting radiation signatures have not been systematically explored. In particular, the polarization signatures, which directly reflect the characteristic strongly dynamical evolution of magnetic field during reconnection, have not been carefully investigated. In this paper, we present a systematic study of radiation and polarization signatures arising from magnetic reconnection in blazars, based on combined PIC and polarized radiation transfer simulations with various physical parameters. We identify a harder-when-brighter trend in the spectral evolution. Moreover, higher-frequency bands (ultraviolet to X-ray) tend to flare earlier than lower-frequency bands (infrared to optical) in the synchrotron spectral component. Most importantly, polarization signatures appear more variable with higher frequencies. We find that the variation in temporal polarization depends strongly on the guide field strength. Specifically, reconnection with a significant guide field component leads to a very high polarization degree that contradicts typical blazar observations, while large polarization angle rotations are unique signatures of magnetic reconnection between nearly antiparallel magnetic field lines. These rotations are at least 90° and can extend to >180°, and they may be in either direction. These results imply that blazars that have shown large polarization angle rotations intrinsically have more nearly antiparallel magnetic field morphology.

Unified Astronomy Thesaurus concepts: Blazars (164); Active galactic nuclei (16); Jets (870); Non-thermal radiation sources (1119); Polarimetry (1278)

1. Introduction

Relativistic jets from active galactic nuclei (AGNs) are among the most extreme astrophysical phenomena in the universe. These plasma jets are powered by the accretion of the supermassive black hole at the center of each AGN. A blazar is a kind of AGN whose jet is directed very close to our line of sight. Their emission is characterized by a two-hump shaped spectral energy distribution (SED) and dominated by non-thermal radiation processes (for a recent review on blazars, see, e.g., Böttcher 2019). The low-energy hump is dominated by synchrotron emission from ultrarelativistic electrons. This is evident by the observed polarization degree (PD), which is consistent with synchrotron emission in a partially ordered magnetic field (Pushkarev et al. 2005; Zhang et al. 2015). The origin of the high-energy hump can be either leptonic or hadronic. In the former case, the high-energy emission comes from the Compton scattering of low-energy photons by the same electrons that produce the low-energy synchrotron component (Marscher & Gear 1985; Dermer et al. 1992; Maraschi et al. 1992; Sikora et al. 1994). In the latter case, the X-ray to γ -ray emission is due to proton synchrotron and/or hadronic cascades (Mannheim 1993; Aharonian 2000; Mücke et al. 2003). The recent very high-energy neutrino detection that is simultaneous with a blazar flare provides the first evidence that the high-energy hump may be of hadronic origins (Aartsen et al. 2018). It has been suggested that high-energy polarimetry, especially the MeV γ -ray polarization

signatures, can diagnose whether the high-energy spectral component is of leptonic or hadronic origin (Zhang & Böttcher 2013; Paliya et al. 2018; McEnery et al. 2019; Rani et al. 2019; Zhang et al. 2019).

The entire blazar spectrum can be highly variable, and the γ -ray bands can flare in as little as a couple of minutes (Aharonian et al. 2007; Albert et al. 2007; Ackermann et al. 2016). Such extreme flares require very fast and efficient particle acceleration within a very small region in space. This localized region is often referred to as the blazar zone. Blazar flares are often interpreted as results of internal shocks that accelerate a large number of nonthermal particles via diffusive shock acceleration (e.g., Marscher & Gear 1985; Böttcher & Dermer 2010; Böttcher & Baring 2019). However, shock models have some trouble in explaining, for instance, the very rapid variability in γ -rays. In recent years, there has been increasing interest in magnetically driven jets, where blazar flares are considered to be driven by magnetic reconnection in the emission region (Giannios 2013; Sironi et al. 2015; Zhang et al. 2018; Giannios & Uzdensky 2019).

Magnetic reconnection is a physical process in a plasma where oppositely directed magnetic field lines rearrange their topology and release a large portion of their magnetic energy. It can be an efficient way to accelerate nonthermal particles if the blazar emission region is considerably magnetized. Numerical simulations including particle-in-cell (PIC) simulations have shown that magnetic reconnection can accelerate both electrons and protons into power-law spectra (Guo et al. 2014, 2016, 2019;

Sironi & Spitkovsky 2014; Werner et al. 2016, 2018; Li et al. 2018b, 2019; Kilian et al. 2020). Depending on how much the reconnection region is magnetized, the nonthermal particle spectra can be either hard or soft, which is consistent with the observed blazar radiation spectra (Guo et al. 2015; Sironi et al. 2015; Petropoulou et al. 2019). Recently, several works have studied the light curves arising from magnetic reconnection, which appear overall to be consistent with blazar observations (Deng et al. 2016; Petropoulou et al. 2016; Christie et al. 2019). However, those works have not yet systematically studied the observable behaviors and trends arising from magnetic reconnection. The issue has three main aspects. First, magnetic reconnection is a highly dynamical plasma process, but its time-dependent radiation signatures have not been well studied. Second, the guide field strength that is crucial to the reconnection dynamics can also strongly affect radiation signatures, but previous works have not studied its effects on radiation. Third, polarization signatures, which can directly reflect the evolution of the intrinsic magnetic field in the reconnection region, remain largely unexplored.

Polarimetry can probe the magnetic field morphology and evolution in astrophysical systems. Since the low-energy component of the blazar spectrum is dominated by synchrotron emission, optical polarization signatures can directly reflect the evolution of the magnetic field in the blazar flaring regions (see Zhang 2019 for a recent review). Although the optical polarization often fluctuates erratically at a low PD during quiescent states, it can reach a higher PD and become strongly variable when the blazar is flaring (Smith et al. 2009; D’Ammando et al. 2011; Ikejiri et al. 2011). In particular, observations have detected large swings in optical polarization angle (PA) simultaneously with multiwavelength blazar flares, indicating significant evolution of the magnetic field (Marscher et al. 2008; Larionov et al. 2013; Blinov et al. 2015). Very interestingly, the RoboPol project has noticed several statistical trends in the optical polarization signatures, such as the PA swings being mostly correlated to γ -ray flares (Angelakis et al. 2016; Blinov et al. 2018). These systematic trends indicate that the polarization variations in blazars originate from physical processes that are not described by completely stochastic random walks (Kiehlmann et al. 2017). It has also been reported by several sources that PA swings can reach far beyond $\sim 180^\circ$, and can take place in both directions in the same blazar (e.g., Marscher et al. 2010; Morozova et al. 2014; Chandra et al. 2015). Furthermore, the PD generally drops during the PA swings (Blinov et al. 2016b). These behaviors indicate that the physical driver of blazar flares with PA swings can strongly alter the magnetic field morphology in the blazar emission region.

PIC simulations have shown that the reconnection layer can fragment, forming a large number of moving plasmoids of different sizes. Such magnetic field morphology and evolution are characteristic of magnetic reconnection and unlike those expected in shocks and turbulence. As a first attempt to identify characteristic signatures of magnetic reconnection, Zhang et al. (2018) have shown that magnetic reconnection in the blazar environment can produce large optical PA swings (beyond 180°), and the PA can swing in both directions during flares. That paper suggests that the PA swings intrinsically originate from the secondary reconnection due to plasmoid mergers, which are unique to magnetic reconnection events. This

illustrates a promising observable constraint with which to identify and diagnose magnetic reconnection events in blazars.

Inspired by the study of Zhang et al. (2018), we perform a series of combined PIC simulations with polarization-dependent radiation transfer simulations. We aim to systematically study the effects on radiation for several key physical parameters, namely, the guide field strength, magnetization factor, radiative cooling, upstream temperature, and observational frequencies. Additionally, we perform our simulation in a larger simulation box to examine whether the radiation signatures are consistent with larger physical sizes. Our goal is to identify general observable patterns of multiwavelength light curves and optical polarization signatures arising from magnetic reconnection in the blazar emission region. In addition, we want to diagnose if specific signatures or trends are shown by various physical parameters of the reconnection layer that could affect the radiation and polarization signatures. Section 2 describes our numerical setup, Section 3 presents the radiation and polarization signatures arising from reconnection with guide fields, Section 4 performs additional parameter studies, and Section 5 discusses the observational implications. We conclude our paper in Section 6.

2. Simulation Setup

The goal of this paper is to systematically study radiation and polarization signatures resulting from magnetic reconnection events in relativistic jets. We assume that the reconnection happens in the blazar zone environment. We start our simulation from a pre-existing current sheet with various initial physical conditions. Then we will investigate how radiation and polarization signatures may depend on the initial physical parameters. The general setups of combined PIC and polarized radiation transfer simulations are the same as in Zhang et al. (2018). In the following, we briefly summarize the setups and describe any additional components to those in Zhang et al. (2018).

2.1. PIC Setup

We perform 2D PIC simulations in the x – z plane using the VPIC code (Bowers et al. 2008), which solves Maxwell’s equations and the relativistic Vlasov equation. The simulations start from a magnetically dominated force-free current sheet, $\mathcal{B} = B_0 \tanh(z/\lambda) \hat{x} + B_0 \sqrt{\text{sech}^2(z/\lambda) + B_g^2/B_0^2} \hat{y}$, where B_g is the strength of the guide field (magnetic field component perpendicular to the reconnecting magnetic field). We set the half-thickness λ of the current sheet to be $0.6\sqrt{\sigma_e}d_{e0}$ in order to have enough particles in the current sheet to carry the electric current to satisfy Ampère’s law, where $d_{e0} = c/\omega_{pe0}$ is the nonrelativistic electron inertial length, $\omega_{pe0} = \sqrt{4\pi n_e e^2/m_e}$ is the nonrelativistic electron plasma frequency, and $\sigma_e = B_0^2/(4\pi n_e m_e c^2)$ is the cold electron magnetization parameter (Guo et al. 2014; Sironi & Spitkovsky 2014). The initial particle distributions are Maxwell–Jüttner distributions with uniform density n_0 and temperature $T_e = T_i$. The simulation assumes an electron–ion plasma with realistic mass ratio $m_i/m_e = 1836$. We expect that our radiation and polarization results should hold for pair plasma and electron–positron–proton plasma, because the leptons consume a significant portion of the dissipated magnetic energy, and the reconnection dynamics and evolution are generally similar (Petropoulou et al. 2019). We use 100 electron–ion pairs in each cell. The

size of the simulation box is $2L \times L$ in the x - z plane. We employ periodic boundary conditions on the x -axis for both fields and particles, while on the z -axis the boundaries are conductive for fields but reflect particles. We insert a long-wavelength perturbation to trigger the magnetic reconnection, which creates a dominating reconnection point located at the center of the simulation box (Birn et al. 2001). The radiative cooling effects are important for blazars. Here we mimic the cooling effect by implementing a radiation reaction force \mathbf{g} , which can be simplified as a continuous friction force for ultrarelativistic particles (Cerutti et al. 2012, 2013),

$$\begin{aligned} \mathbf{g} &= -\frac{\mathcal{P}_{\text{rad}}}{c^2}\mathbf{v} \\ &= -\frac{2}{3}r_e^2\gamma\left[\left(\mathbf{E} + \frac{\mathbf{u} \times \mathbf{B}}{\gamma}\right)^2 - \left(\frac{\mathbf{u} \cdot \mathbf{E}}{\gamma}\right)^2\right]\mathbf{u} - \frac{4}{3}\sigma_T\gamma\mathcal{U}_*\mathbf{u}, \end{aligned}$$

where $\mathbf{u} = \gamma\mathbf{v}/c$ is the four-velocity, \mathcal{P}_{rad} is the radiation power, $r_e = e^2/m_ec^2$ is the classical radius of the electron, and \mathcal{U}_* is the photon energy density (also see Zhang et al. 2018 for implementation details in VPIC). Since nonthermal electrons in the blazar emission region are highly relativistic, the non-relativistic terms in the radiation reaction force are not included in our simulations (Cerutti & Beloborodov 2017).

We choose simulation parameters according to the physical conditions inferred from spectral modeling of the observations of flat-spectrum radio quasars (FSRQs), which exhibit the strongest flux and polarization variability (Ackermann et al. 2016; Angelakis et al. 2016). We choose the plasma thermal temperature $T_e = 100m_ec^2$ for our default run. This is below the low-energy cutoff (ranging from hundreds to thousands of m_ec^2 , see, e.g., Böttcher et al. 2013; Paliya et al. 2018) of the nonthermal electron spectra inferred for FSRQs, enabling the simulations to capture the formation of nonthermal electron spectra. Spectral fitting for FSRQs suggests that the high-energy cutoff of the electron spectrum is $\gamma \sim 10^4$ (Böttcher et al. 2013; Paliya et al. 2018). Since the high-energy cutoff is roughly equal to the electron magnetization factor σ_e (e.g., Guo et al. 2014), we choose $\sigma_e = 4 \times 10^4$ for our default run. This corresponds to a total magnetization $\sigma_0 \approx (m_e/m_i)\sigma_e \approx 22$.

The radiative cooling plays an important role in blazar radiation and polarization signatures. However, since the physical scale of the PIC simulation is very small compared to the realistic blazar zone, we need to normalize the cooling rate by the acceleration rate in PIC simulations so that they can produce similar light curves to observations. Although the exact particle acceleration mechanism in magnetic reconnection is a very complicated issue and beyond the scope of this paper, we only need the acceleration rate as a normalization for the cooling rate. For simplicity, we take the results from recent analyses of PIC simulations on the acceleration rate (Guo et al. 2014, 2015; Li et al. 2019), which have shown that the acceleration rate $\alpha = \dot{\gamma}/\gamma$ scales with $\sqrt{\sigma_e}$. Based on their measurement, we determine that the particle acceleration rate is approximately $\alpha = \dot{\gamma}/\gamma \approx \sqrt{\sigma_e}\omega_{pe0}/2000$. The particle cooling timescale is given by $\tau_{\text{cool}} = 3t_0/(2\gamma\sigma_e\tilde{r}_e)$ (Zhang et al. 2018), where $t_0 = \omega_{pe0}^{-1}$ and $\tilde{r}_e = r_e/ct_0$. For FSRQs, the cooling time τ_{cool} is usually longer than the acceleration time. Previous works have used the value of γ_{rad} where the acceleration and cooling timescales are equal to normalize the cooling effects (Cerutti et al. 2016). However, this choice

Table 1
List of PIC Simulations

Run	B_g/B_0	σ_e	T_e/m_ec^2	C_{10^4}	L_x/d_{eo}
DEF	0.2	4.0×10^4	100	200	1.6×10^4
GF1	0.0	4.0×10^4	100	200	1.6×10^4
GF2	0.4	4.0×10^4	100	200	1.6×10^4
GF3	0.6	4.0×10^4	100	200	1.6×10^4
GF4	1.0	4.0×10^4	100	200	1.6×10^4
MF1	0.2	10^4	100	200	1.6×10^4
MF2	0.2	1.6×10^5	100	200	1.6×10^4
CF1	0.2	4.0×10^4	100	100	1.6×10^4
CF2	0.2	4.0×10^4	100	400	1.6×10^4
UT1	0.2	4.0×10^4	400	200	1.6×10^4
BS1	0.2	4.0×10^4	100	200	3.2×10^4

Note. All PIC simulation parameters. There are 11 PIC runs in total: DEF is the default parameter set, GF1–GF4 are for different guide fields, MF1 and MF2 are for different magnetization factors, CF1 and CF2 are for different cooling factors, UT1 is for a higher upstream temperature, and BS1 is for a larger box size. We consider the following parameters: B_g/B_0 is the ratio between the guide field component and the antiparallel magnetic field component, σ_e is the electron magnetization factor, T_e is the upstream temperature of particles, $C_{10^4} \equiv \alpha\tau_{\text{cool}}$ for electrons with $\gamma = 10^4$, and L_x/d_{eo} is the simulation box width in units of d_{eo} .

often leads to very strong cooling, which does not fit with typical FSRQ parameters (Yuan et al. 2016). To capture the cooling effects in the simulation time, we adjust τ_{cool} so that $C_{10^4} \equiv \alpha\tau_{\text{cool}} = 200$ for electrons with $\gamma = 10^4$ in the default run. As shown in the following, the resulting radiation and polarization signatures are in good agreement with observations. In principle, the coolings due to synchrotron and Compton scattering are different. However, for typical FSRQs, the two cooling timescales have very similar expressions, except that the former is proportional to the magnetic energy density, while the latter is proportional to the photon energy density. The exact ratio of the two energy densities only matters when we study the multiwavelength radiation signatures. In this paper, we focus on the synchrotron signatures, thus we only consider the synchrotron cooling term in our simulations.

For the default run, $L_x = 2L = 1.6 \times 10^4 d_{eo}$ and $L_z = L = 8 \times 10^3 d_{eo}$, which is normalized to $\sim 8.5 \times 10^{10}$ cm in typical FSRQs ($B \sim 0.1$ G, $n_e \sim 0.01$ cm $^{-3}$). While this is much smaller than the typical blazar emission region ($\sim 10^{16}$ cm), we find that the general plasmoid dynamics are qualitatively the same with domain size 2× larger than the present case (refer to the BS1 simulation in Section 4). Since the key mechanism in producing radiation signatures is the plasmoid coalescence/merger, as demonstrated in this paper, this suggests that the underlying process is robust even on the macroscopic scales over which blazar flares take place. We choose a simulation grid size of 4096×2048 for the default run, so that the cell sizes $\Delta x = \Delta z \sim 0.32d_e$ can resolve the thermal electron inertial length $d_e = \sqrt{\gamma_0}d_{eo}$, where $\gamma_0 = 1 + 3T_e/2m_ec^2 \sim 150$. We use the same Δx and Δz for all runs. Table 1 shows the simulation parameters for all the 11 runs. We name the default run DEF, and it has a guide field $B_g/B_0 = 0.2$. We vary the guide field from 0.0 to 1.0 (GF1–GF4) to study how the guide field changes electron acceleration and radiation signatures. We compare the default run with runs with different magnetization factors σ_e (MF1 and MF2) and cooling factors

C_{10^4} (CF1 and CF2), higher upstream plasma temperature (UT1), and larger box size (BS1).

2.2. Radiation Transfer Setup

Since the reconnection simulation is performed in the x - z plane in the VPIC code, we fix our line of sight in the comoving frame of the simulation box along the y -axis. This is because in our 2D PIC simulations, the evolution and morphology of the guide field component, which is the magnetic field component in the y direction, are not resolved. Since the synchrotron emission depends only on the magnetic field perpendicular to the line of sight, setting the line of sight along the y -axis can eliminate the effects of untracked guide field distribution and evolution on the synchrotron radiation signatures. We choose that the reconnection layer is moving in the z -direction with a bulk Lorentz factor $\Gamma = 10$ in the observer's frame for all our simulations. Therefore, the Doppler factor in the observer's frame is $\delta = \Gamma = 10$, which is a typical number for blazars. We normalize the initial antiparallel magnetic field components in the reconnection plane (i.e., without the guide field) to be 0.1 G, which is a typical value found in leptonic blazar spectral fitting (Böttcher et al. 2013; Paliya et al. 2018).

To obtain the particle distributions and magnetic fields, we reduce every 16×16 PIC cells into one radiation transfer cell. We find this resolution is adequate to capture all relevant radiation features and provide enough statistics to obtain smooth particle spectra in each radiation transfer cell. We divide the particle kinetic energy $(\gamma - 1)m_e c^2$ evenly into 100 bins in logarithmic space between 10^{-4} and 10^6 . Then we obtain the particle spectra by counting the number of particles in each energy bin. We calculate the magnetic field in the radiation transfer cell by averaging the fields in the 16×16 PIC cells. As we can see in all snapshots in Sections 3 and 4, the magnetic field does not show very sharp changes on very small scales. Additionally, plasmoids smaller than 16×16 PIC cells contain a very limited number of nonthermal particles. Thus averaging the magnetic field in the 16×16 PIC cells does not lose any major observable signatures. Since we use a periodic boundary in the PIC simulations, we find that the motion of plasmoids in our simulations is generally nonrelativistic. Therefore, we do not include any local Lorentz factor in our radiation transfer simulations.

We use the 3DPol code developed by Zhang et al. (2014) to perform radiation transfer simulations. This code is a polarization-dependent radiation transfer code for synchrotron emission. It evaluates the Stokes parameters of the synchrotron emission (Stokes parameters represent the polarization status in the emission) from each cell in the simulation, so as to include all linear polarization signatures, based on the magnetic field and particle distributions, which are obtained from the PIC simulations. It then traces the emission beams to the plane of the sky, and adds up all emission in the same cell on the plane of the sky within the same frequency band that arrives in the same time step. Since the line of sight in our simulation is set to be along y -axis, the plane of the sky is then parallel to the x - z plane. The code has time, space, and frequency dependences. A key feature of the 3DPol code is that it allows us to get the polarized emission maps at every time step. This feature can illustrate the surface brightness and polarization distributions in the simulation domain, so that we can pinpoint the plasma dynamics with resulting radiation behaviors.

3. Radiation and Polarization Signatures from Magnetic Reconnection

Zhang et al. (2018) have presented the radiation and polarization signatures arising from magnetic reconnection between perfectly antiparallel magnetic fields, in which we have found strong PA swings. Here we present additional simulations to understand how different physical parameters may affect the radiation and polarization signatures. We recognize that in relativistic jets, current sheets may form via magnetic instabilities/turbulence or striped jets (Begelman 1998; Giannios & Spruit 2006; Giannios & Uzdensky 2019). In the former case, we expect that the reconnecting magnetic field lines are unlikely to be perfectly antiparallel, but will have a finite guide field component; in the latter case, the oppositely oriented magnetic stripes are initially formed at the central engine due to magnetic irregularities that are advected into the jet. Depending on the magnetic structure at the central engine, the reconnecting magnetic field lines may or may not be perfectly antiparallel. Guide fields can considerably affect the magnetic reconnection dynamics (Lyubarsky 2005; Liu et al. 2015, 2020; Ball et al. 2019; Rowan et al. 2019). Furthermore, different observational frequencies may also lead to different spectral and temporal patterns in both radiation and polarization signatures. In this section, we present general radiation and polarization signatures from magnetic reconnection with a finite guide field, and study the effects of observational frequency and guide field strength.

3.1. General Temporal and Spectral Behaviors

We set up the reconnection layer with an initial electron magnetization factor of $\sigma_e = 4 \times 10^4$ with a guide field of $B_g/B_0 = 0.2$ (see Table 1 DEF for physical parameters). Since we use the real mass ratio between protons and electrons, this yields a total magnetization factor of $\sigma_0 \sim 22$. Figures 1 and 2 present the temporal and spectral radiation signatures, respectively.

We trigger the magnetic reconnection with a small initial perturbation. From the light curve (Figure 1, top panel), we can see that the reconnection starts to accelerate particles to high Lorentz factors around $t \sim 0.3\tau_{lc}$, where $\tau_{lc} \equiv L_x/c$ is the light-crossing time. Figure 3 plots snapshots of spatial distributions of magnetic field strength, nonthermal particles, and polarized emission maps in the simulation domain. The four snapshots correspond to the rising phase of the first flare in the light curve, the peak of the second and third flares, and the saturation of magnetic reconnection. We can clearly observe that soon after the trigger of reconnection, the reconnection layer fragments into a series of plasmoids (Figure 3, left three panels). These plasmoids are quasi-circular structures in our 2D simulation. They are pervaded by magnetic field loops with a high density of nonthermal particles. The direction of plasmoid magnetic field loops is clockwise, due to the initial choice of the magnetic field topology, where the upper half of the simulation domain has a magnetic component in the reconnection plane along the $+x$ direction, while the lower half has it along the $-x$ direction. As we can see in the following, this choice does not affect the development of reconnection or the radiation and polarization signatures.

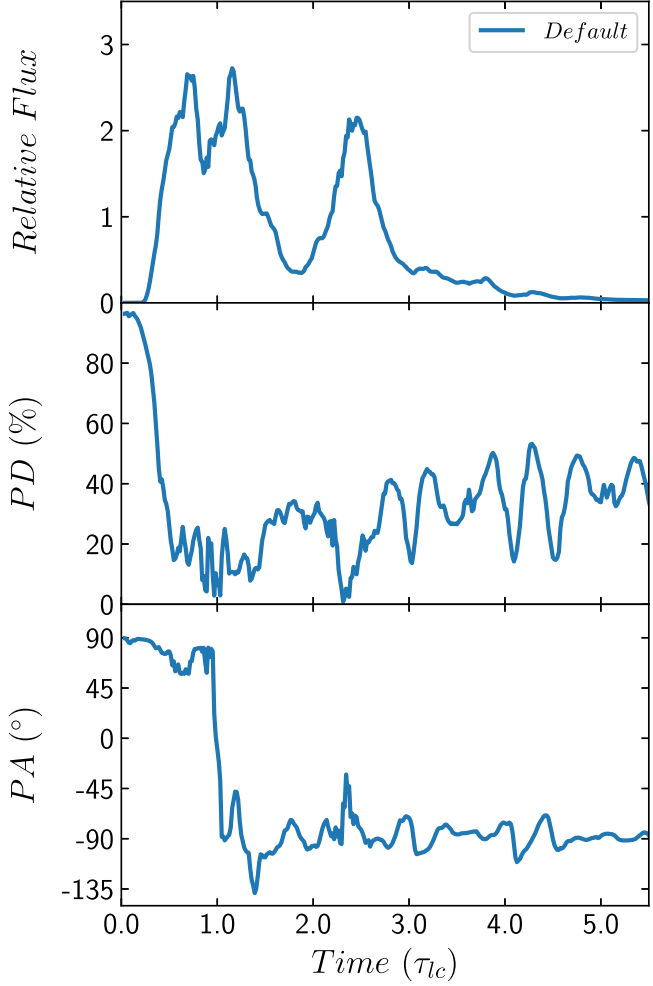


Figure 1. From top to bottom: optical light curve, PD, and PA for our default setup. Time is in units of the light-crossing time ($\tau_{lc} \equiv L_x/c$) of the simulation box length. The light curve is plotted in relative flux. All results are presented in the observer’s frame.

3.1.1. Temporal Patterns

We find that the plasmoids produced in the reconnection layer generally move away from the main X-point. But they can have different bulk speeds, so they may collide and merge into each other. Since all plasmoids produced from the primary reconnection have clockwise magnetic fields (if the initial morphology were reversed, then magnetic fields in the plasmoids would all point in the counterclockwise direction), when they collide and merge, they form a current sheet at the contact region and trigger secondary reconnection (see Figure 4 for the evolution of a merger event). The first flare is because the primary reconnection accelerates a large number of nonthermal particles. We find that the small fluctuations/spikes on the light curves originate from mergers of smaller plasmoids. On the other hand, the second and third flares are due to large plasmoid mergers. After the third flare, the magnetic energy in the reconnection layer has largely been depleted, and there is only one remaining large plasmoid, due to our periodic boundary condition, which passively cools. Therefore, there are no additional flares afterwards.

Before the reconnection starts, since the PA has 180° ambiguity, the initial antiparallel magnetic field components appear to have the same polarization signatures as a uniform

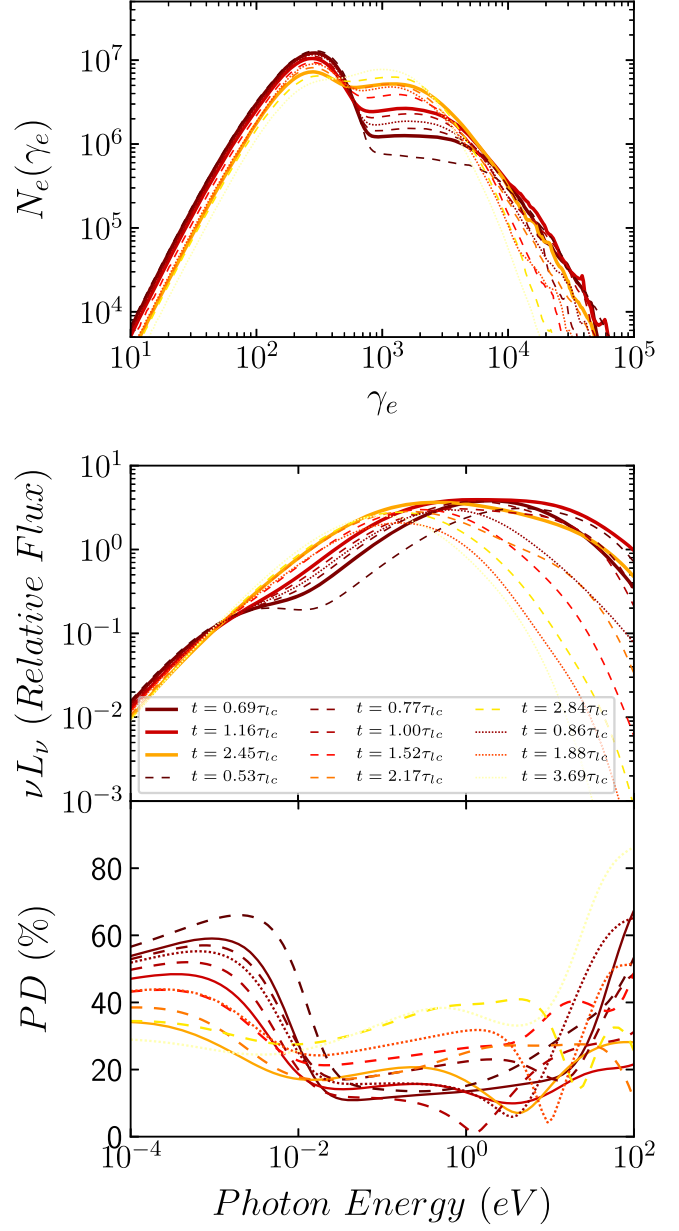


Figure 2. From top to bottom: snapshots of particle spectra, SEDs of the synchrotron component, and frequency-dependent PDs. SEDs are plotted in relative flux. The first three bold solid lines are snapshots chosen at the peak of the light curve, the following six dashed lines are in between, the last three dotted lines are snapshots in the valleys (readers can refer to Figure 1 for the exact location). All results are presented in the observer’s frame.

field. For the same reason, the clockwise and counterclockwise magnetic field loops in the plasmoids look the same as rings of magnetic field lines. Additionally, only the magnetic field components that are perpendicular to the line of sight contribute to synchrotron emission. Therefore, we see nearly 100% PD at the beginning of the simulation. Soon after the reconnection starts, the reconnection layer fragments into many plasmoids, making the overall magnetic field morphology very disordered. Thus we observe that the PD quickly drops to $\lesssim 20\%$ when the flux becomes considerable (Figure 1, top and middle panels). Figure 3 shows that a significant amount of polarized emission comes from plasmoids, which have a high density of energetic particles and stronger magnetic fields. We can see that the polarized emission from the plasmoids has the

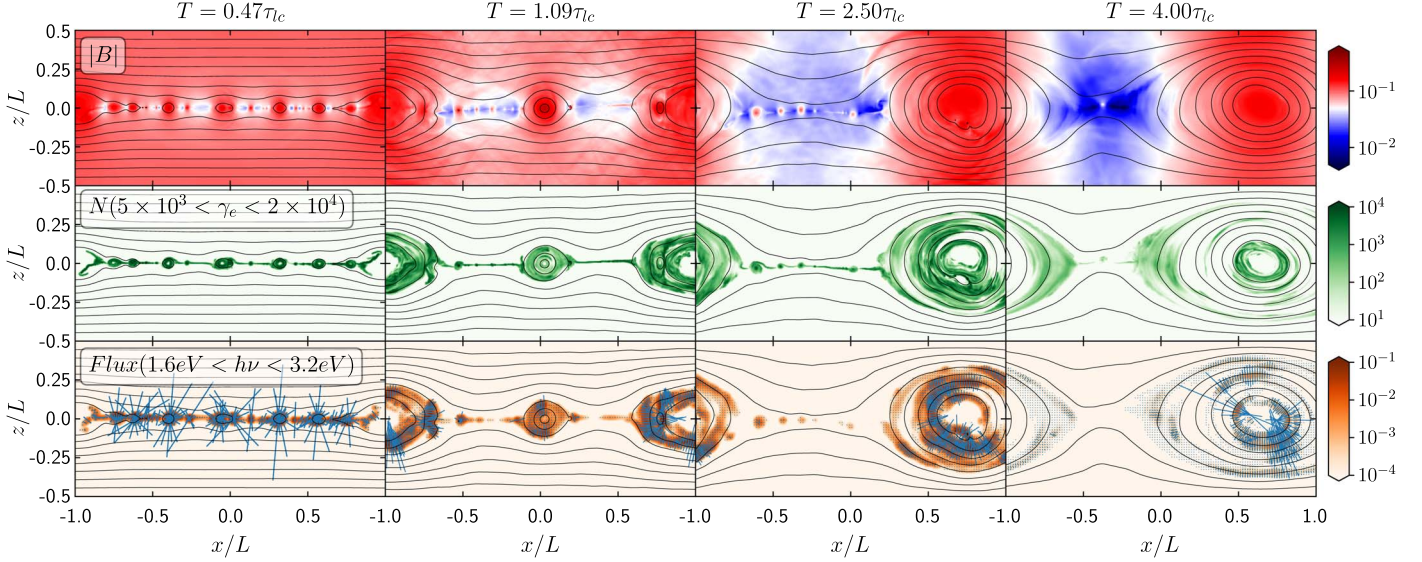


Figure 3. Snapshots of the evolution of reconnection for the default setup. The first row is the magnetic field strength, which is plotted using the resolution of the original PIC simulation, 4096×2048 . The second row is the spatial distribution of nonthermal particles within the given range of Lorentz factor. It is plotted after the reduction of 16×16 PIC cells, at the resolution of 256×128 . The third row is the resulting polarized emission maps in the given observational band. The black lines in all panels trace the magnetic field lines. The blue dashes in the third row represent the local polarized flux; their lengths are proportional to its amplitude, and their directions illustrate the local PA.

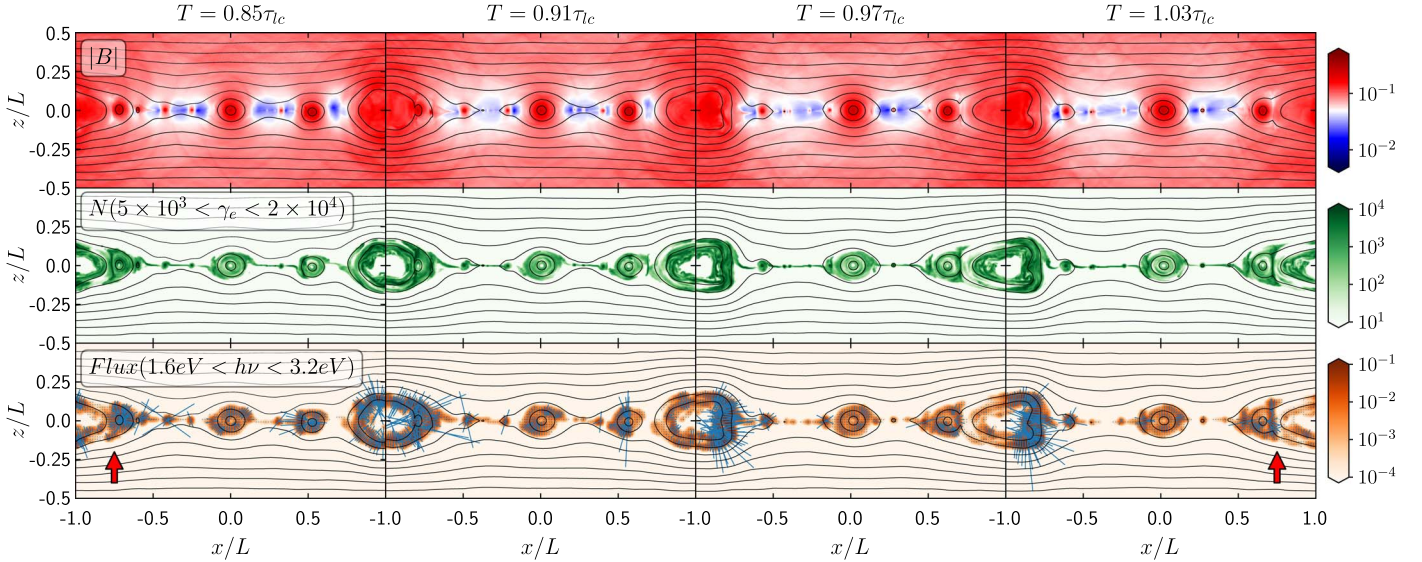


Figure 4. Same as Figure 3, but these snapshots trace the evolution of a large plasmoid merger event (at the left end of the simulation domain marked by a red arrow) in the default run. In the last snapshot, there is a large plasmoid merger starting at the right end of the simulation domain (also marked by a red arrow).

PA generally perpendicular to the magnetic field loops. Given that the magnetic field of plasmoids is approximately circular and that they frequently collide with each other, the overall magnetic field morphology during reconnection is disordered and variable. Since the reconnecting magnetic field lines are in the $\pm x$ directions, the overall emission has an excess contribution from the $\pm x$ magnetic field components. As a result, we observe that PD remains at $\lesssim 20\%$ and PA fluctuates around a mean value at $\pm 90^\circ$ (they are the same angle due to the 180° ambiguity, representing $\pm x$ magnetic field components).

The situation changes when large plasmoids merge into each other. Since plasma is strongly compressed when plasmoids merge (Li et al. 2018a), the secondary reconnection at the merging site accelerates more nonthermal particles. This causes its emission to dominate over that from other parts of the

reconnection layer. Consequently, the temporal PD and PA variations during this period represent the evolution of the plasmoid merger. Figure 4 tracks a plasmoid merger event at the left end of the simulation box during the large PA rotation between $t = 0.85\tau_{lc}$ and $t = 1.05\tau_{lc}$ (the rising phase of the second flare). Clearly, we observe a large number of nonthermal particles accelerated in the contact region. These newly accelerated particles can stream along the magnetic field lines of the two merging plasmoids, and thus light up the magnetic field morphology at their location. However, the numbers of particles that are streaming clockwise and counterclockwise are not the same. This is very similar to the primary reconnection layer. As we can see in Figure 3 and snapshots of all other simulations, plasmoids and nonthermal particles that are produced to the left are generally not

symmetric to those at the right. Consequently, at the secondary reconnection layer in the larger plasmoid mergers, if there is a considerable difference in the flow of particles between the clockwise and counterclockwise directions, the PA will show a smooth rotation representing the dominant direction. On the other hand, if the two outflows are comparable in the secondary magnetic reconnection, we do not expect a PA rotation. Nevertheless, in either situation there should be strong particle acceleration at major plasmoid mergers, so that we always expect a flare event. As we can see in the first three snapshots in Figure 4, the large plasmoid merger on the left side of the reconnection layer has more nonthermal particles in the counterclockwise direction, thus the PA makes a smooth and fast swing from 90° to -90° . In the last snapshot, there is another large plasmoid merger starting on the right. Although this one also has a counterclockwise preference, its initial PA position is different from the final PA position of the previous one. This leads to a jump of PA at $t = 1.05\tau_{lc}$, followed by a continuous PA swing to -135° . On the other hand, the large plasmoid merger that leads to the third flare gives similar number of nonthermal particles streaming in each direction. Therefore, we do not observe a PA swing associated with this flare.

3.1.2. Spectral Properties

Magnetic reconnection quickly accelerates electrons into a power-law distribution. Due to the synchrotron cooling, the particle spectra exhibit a broken power-law shape (Figure 2, top panel). The optical emission plotted in Figure 1 is beyond the cooling break. Very interestingly, we observe an overall harder-when-brighter trend for the cooling spectra (see Figure 2, middle panel; solid lines are always harder than dotted lines, while dashed lines are in between). This is because at the flare peak, where the primary reconnection and later on the large plasmoid mergers have the highest efficiency, the accelerated particle power-law distribution is very hard. It is also evident from Figure 2 that the part of the nonthermal particle spectrum that does not suffer from strong cooling ($10^5 < \gamma_e < 4 \times 10^3$) is very hard. Then the radiative cooling gradually softens the spectra after the flare peak, which results in an overall harder-when-brighter trend. We also find that the PD tends to be lower at the flare peak than the lower flux states (Figure 2, bottom panel). This is because more plasmoids are produced and merge when the flux is higher, leading to more disordered magnetic field morphology in the reconnection layer. We observe that the PD is very high toward the low and high ends of the spectra. The high-energy end is easily understandable, because there are very few very high-energy particles. The high PD at lower energies, however, is due to the fact that the low-energy emission originates from upstream thermal particles. These particles occupy the entire reconnection layer, including the very ordered magnetic field structure at the top and bottom of it. Nonetheless, this part of the emission is not expected to be observed, because the low-energy emission shows very low flux and never flare during the reconnection development.

3.2. Effects of Observational Frequencies

In light of the harder-when-brighter trend, we expect that the radiation and polarization signatures can depend on observational bands. Figure 5 plots light curves and temporal variations in PD and PA for infrared, optical, and ultraviolet bands. They

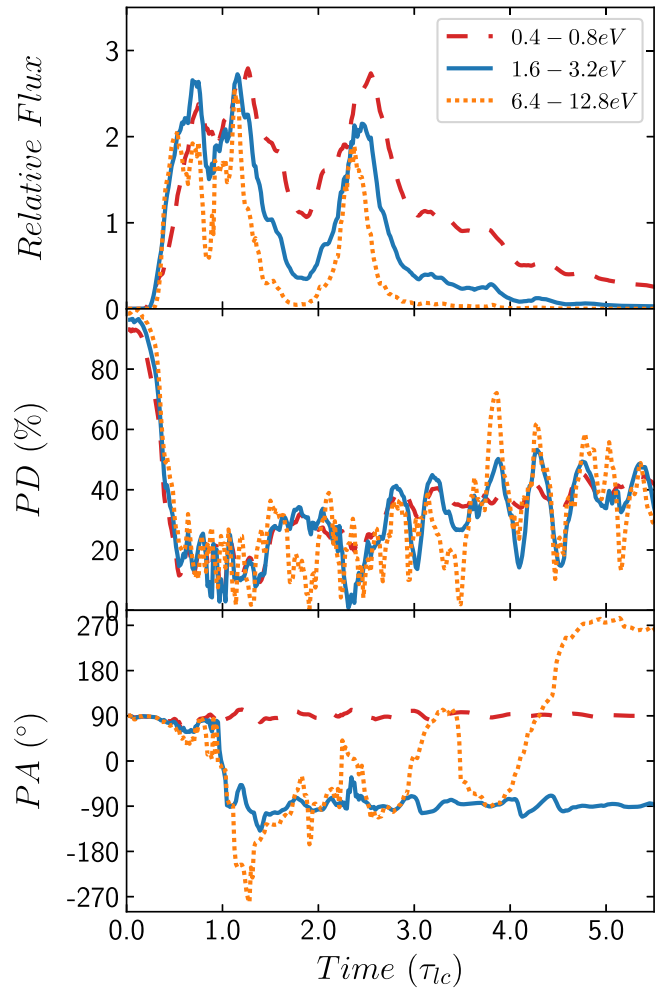


Figure 5. From top to bottom: light curves, temporal PD, and PA for three different bands—infrared, optical, and ultraviolet—for the default run; the bands are separated by factors of four in photon energy as shown in the legend.

generally represent three positions in the spectrum (refer to Figure 2), namely, around the cooling break (infrared), in the cooling spectrum (optical), and near the spectral cutoff (ultraviolet). We find several interesting patterns in the light curves. One is that the higher-energy bands tend to flare earlier than the lower-energy bands. This is because the number of higher-energy particles peaks at the maximal efficiency of magnetic reconnection during plasmoid mergers. Since the magnetic field lines are nearly antiparallel in the contact region of the two merging plasmoids, the acceleration is most efficient and can accelerate the highest-energy particles. As the merging moves beyond the contact region, it can no longer accelerate these particles. Additionally, the synchrotron losses cool down these highest-energy particles. Since the cooling is proportional to the electron energy, it is slower at lower energies, so electrons can continue to accumulate even if the reconnection efficiency drops, resulting in a delay in the flare peak. This can be seen clearly in Figure 6, where the highest-energy particles that are responsible for the UV emission mostly exist near the X-point and merging contact region, while lower-energy particles cover a larger spatial region in the reconnection layer. Another feature is that the higher-energy bands show more spikes in the light curve than the lower-energy bands. Additionally, we find that the flare amplitude, which we define as the ratio of the flare peak to the flux after the saturation of

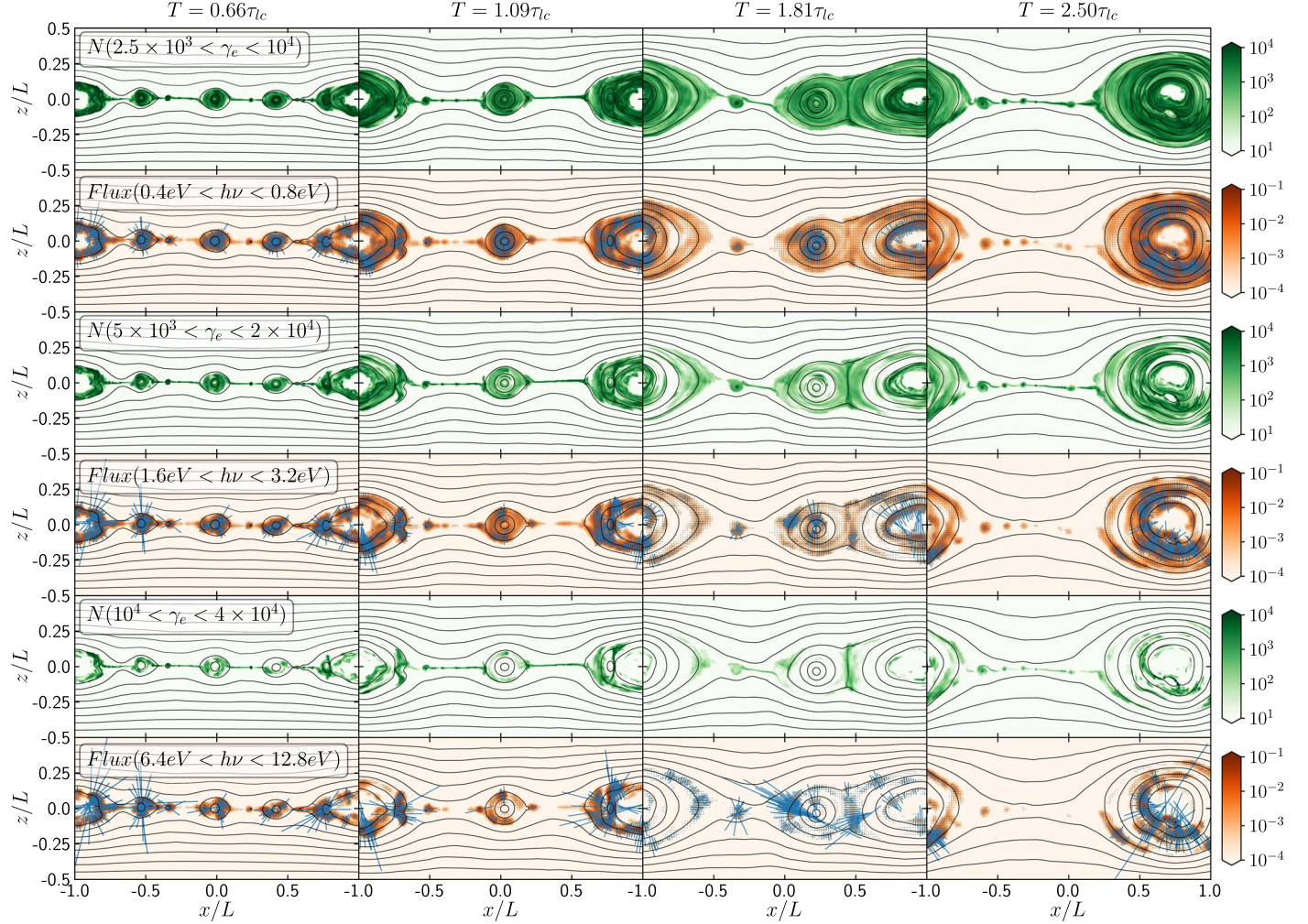


Figure 6. Snapshots of particle spatial distributions of different Lorentz factors and polarized emission maps in corresponding observational bands. The magnetic field snapshots are not plotted, because they are the same for different observational bands.

reconnection (saturation is at $\sim 3\tau_{lc}$ in Figure 5), is much larger for higher-energy bands. Apparently, both patterns can be attributed to the fact that high-energy particles are short-lived compared to low-energy ones. As we can see in Figure 6, high-energy particles are present only at the formation of relatively large plasmoids or during major plasmoid mergers. At other times, they cool very fast and are very limited in number. However, at their respective peaks, the maximal flux of the higher-energy bands is not significantly lower than that of the lower-energy bands, thus the higher-energy bands exhibit larger flare amplitude and more spikes than the lower-energy bands.

The average PDs between different observational bands appear very similar. However, higher-energy bands are more variable than lower-energy ones. This is more clearly illustrated in the time-dependent PA evolution, where one can see much stronger variations: in particular, large PA swings in the ultraviolet. These features are directly related to the spatial distribution of nonthermal particles. Owing to the fast synchrotron cooling, high-energy particles are mostly in very localized regions near the plasmoid merging sites (Figure 6, fifth row), and can only survive for a short period of time. As a result, their emission represents the highly dynamical evolution of plasmoid merger events, leading to strongly variable PD and PA. On the other hand, low-energy particles can survive for

longer, so they are distributed in much larger regions in the neighborhood of the reconnection layer (Figure 6, first row). Since the reconnection region has relatively disordered magnetic field structure, the emission by these uncooled particles can contaminate the polarization signatures from large plasmoid mergers. As a result, even the polarized flux from the large plasmoid mergers is not very dominant compared to other parts of the reconnection region (Figure 6, second row, where the relative polarized flux represented by the length of blue dashes is shorter than in the last row). Therefore, their resulting PD and PA represent the overall evolution of the reconnection layer, which is less variable. Nonetheless, in either case the reconnection plane has very disordered magnetic field morphology, thus the average PDs between different bands are very similar. We notice that after the reconnection saturates at $\sim 3\tau_{lc}$, the ultraviolet band still shows PA rotations. This is because, although reconnection has saturated, a few small plasmoids are still generated occasionally, which can merge with the large plasmoid at the periodic boundary. Due to the strong cooling for these high-energy particles, the emission from the reconnection layer is completely dominated by these small flashes from small plasmoid mergers. This explains why we do not see these signatures in infrared and optical bands, whose emission is dominated by the uncooled particles that contaminate the

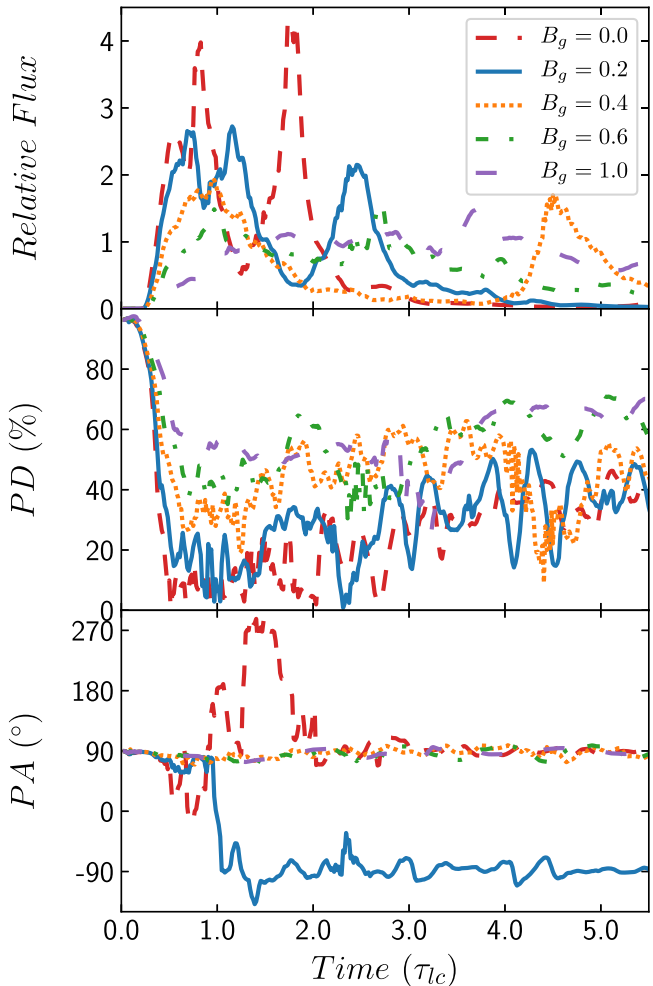


Figure 7. From top to bottom: optical light curves, temporal PD, and PA for different guide fields (they are GF1, default run, GF2, GF3, and GF4; B_0 is dropped in the legend).

polarization signatures. Nonetheless, after the reconnection saturates, the flux in all bands is very low, so these polarization signatures should not be observed.

3.3. Effects of the Guide Field Strength

As shown so far, the time-dependent radiation patterns, especially the polarization signatures, are strongly dependent on the plasmoid motion and mergers. The strength of the guide field plays an essential role in the production and evolution of plasmoids (e.g., Ball et al. 2019; Liu et al. 2020). Here we investigate how radiation and polarization signatures can depend on the guide field. Figure 7 shows the results. We can immediately observe several trends here. First, the flare duration, including both individual variability timescale and the overall duration, is shorter for smaller guide fields. Second, the flare amplitude is higher for smaller guide fields (Guo et al. 2020b). In the most extreme case where $B_g/B_0 = 1.0$, the flare amplitude is less than doubled, clearly showing that acceleration of reconnection is not efficient with large guide fields. Most importantly, we see that the average PD is higher for larger guide fields. In particular, the average PD for $B_g/B_0 \gtrsim 0.5$ is very high, at $\gtrsim 40\%$ throughout the evolution of reconnection. Given their low flare amplitudes and very high PD, we suggest that magnetic reconnection with a large guide

field is unlikely to be responsible for typical blazar variability. Interestingly, for any guide field strength, the PD is always variable. Lastly, we observe that the PA swings are only present when the guide field is small. Specifically, the case $B_g = 0$ exhibits very strong PA rotations, which is consistent with our previous work (Zhang et al. 2018).

The above observational trends originate from the difference in plasmoid production and mergers for different guide field strengths. Comparing the default case (Figures 3, 4, and 6) with different guide field simulations (Figures 8–11), we can clearly see that the development of reconnection is slower for larger guide fields. This explains the longer flare duration for cases of larger guide field. Additionally, more magnetic energy is dissipated to accelerate nonthermal particles in the cases of smaller guide field, since there are more nonthermal particles for smaller guide fields (middle row in Figures 8–11). Apparently, how fast the magnetic energy is dissipated depends on the guide field strength. Consequently, we observe higher flare amplitudes for smaller guide fields (Guo et al. 2020b).

Most importantly, the numbers of plasmoids and plasmoid mergers, are anticorrelated to the guide field strength. This is because a finite guide field can slow down the formation of secondary magnetic islands by preventing the reconnection exhausts from collapsing (Liu et al. 2020). As clearly illustrated in Figures 8–11, the number of plasmoids at a particular time in the simulations is larger with smaller guide fields. Specifically, for $T = 1.09\tau_{lc}$ and $T = 1.81\tau_{lc}$, we can see that the cases $B_g/B_0 = 0.4–1.0$ (GF2–GF4) have very little or no new plasmoid production, but for smaller guide fields ($B_g/B_0 = 0$ and 0.2, GF1 and default run) there is still some plasmoid production and/or merger events. Furthermore, we find that the plasmoid mergers are also weakened by the strong guide field, which reduces the nonthermal particle acceleration at the secondary reconnection site and slows down the overall merger process. We can easily see in the third column of Figures 4 and 8, where large plasmoid mergers are ongoing, that the polarized flux from the merger site is very dominant in both cases (refer to the lengths of the blue polarized flux dashes in the third rows). In contrast, the polarized flux from plasmoid mergers is not dominant for larger guide field strengths. This is clearly shown in the last column of Figures 10 and 11. Consequently, even when large plasmoid mergers happen in a reconnection layer with considerable guide field components, they cannot lead to large PA rotations. Finally, the production of plasmoids and their mergers make the overall magnetic morphology very disordered, resulting in lower PD with smaller guide fields. Nonetheless, considering that the reconnection is a violent process that significantly alters the magnetic field structure, the PD is always variable for any guide field strength, which represents the evolution of plasmoids in the reconnection plane.

4. Additional Parameter Studies

In the previous section, we have shown that the magnetic reconnection exhibits profound radiation and polarization signatures in different observational bands, which are due to the location of the specific band in the synchrotron-cooled spectrum. Additionally, we find that guide field strengths can strongly affect the reconnection dynamics and the resulting emission. In this section, we perform additional parameter studies to understand how radiation and polarization signatures can depend on other physical parameters in the reconnection

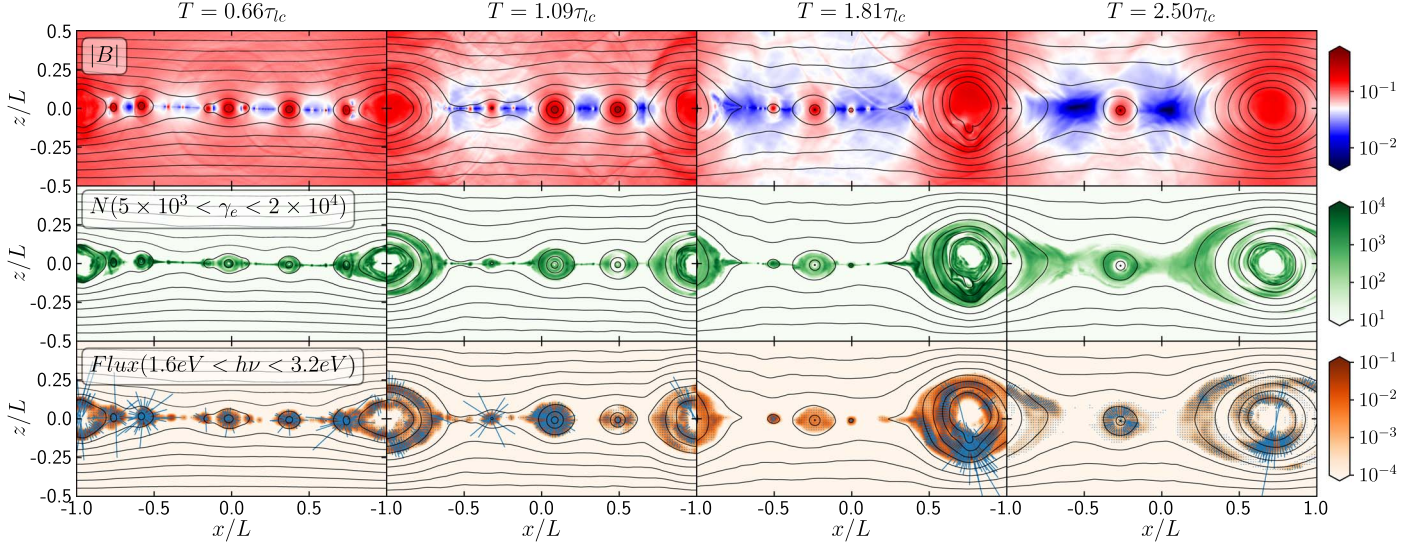


Figure 8. Snapshots of the spatial distributions of magnetic field strengths, nonthermal particles, and polarized emission for the run GF1 ($B_g = 0.0$). Blue dashes in the third row represent the relative flux and PA of the polarized emission in each cell.

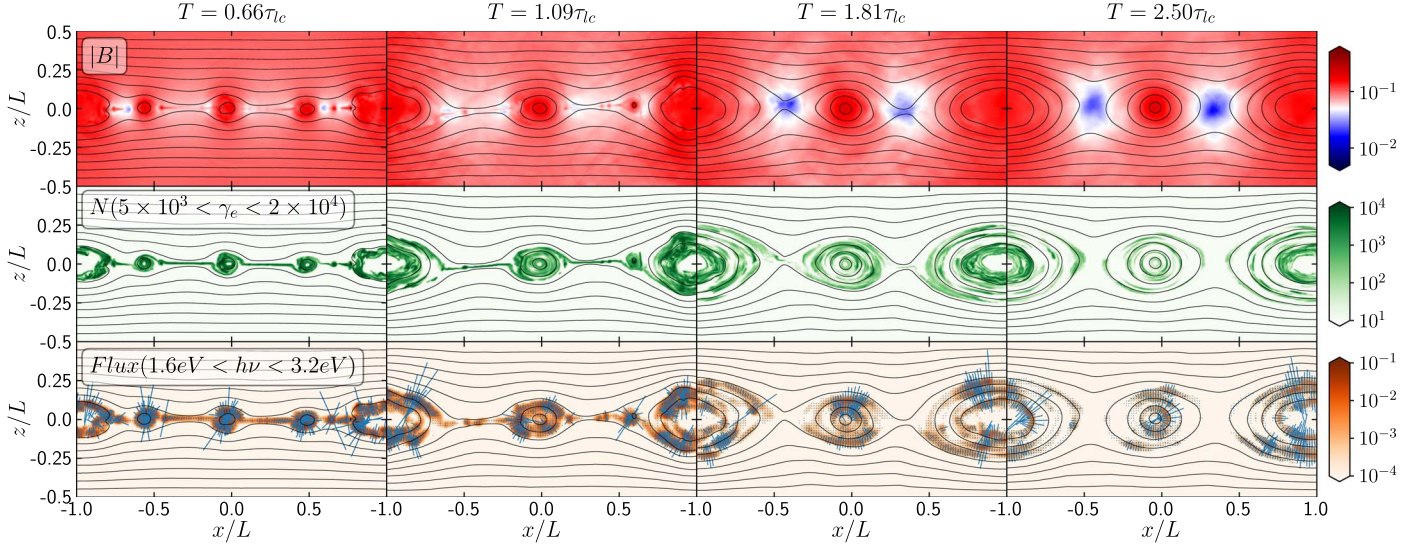


Figure 9. Same as Figure 8 but for the run GF2 ($B_g/B_0 = 0.4$).

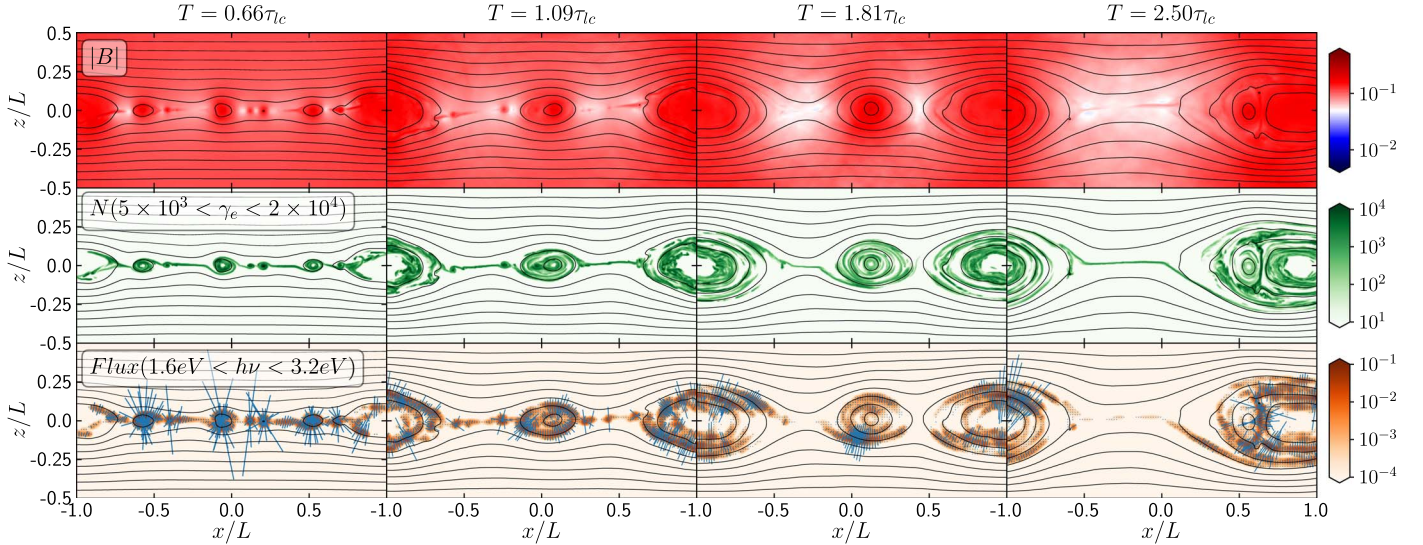


Figure 10. Same as Figure 8 but for the run GF3 ($B_g/B_0 = 0.6$).

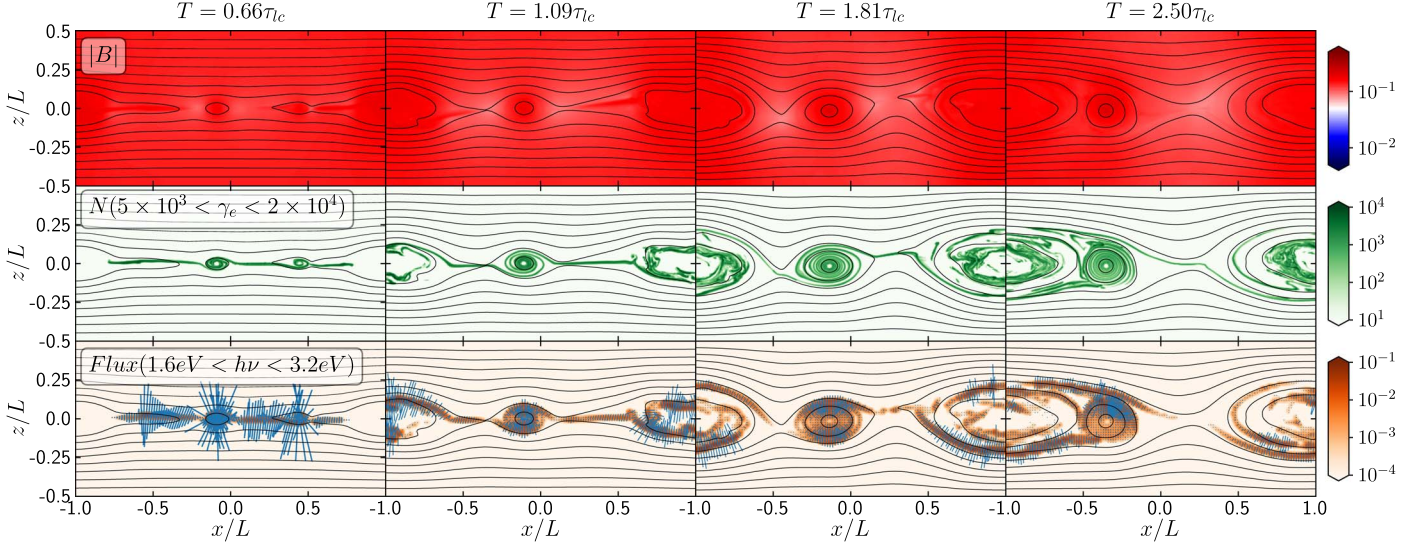


Figure 11. Same as Figure 8 but for the run GF4 ($B_g/B_0 = 1.0$).

region. These parameters are the magnetization factor (σ), the cooling factor, and the upstream electron temperature. The magnetization factor is clearly a very important parameter that affects the reconnection dynamics, as shown by many previous studies (Guo et al. 2014; Sironi & Spitkovsky 2014; Petropoulou et al. 2016). The cooling factor in our simulation is a free parameter that affects the radiative cooling of particles, which may result in observable signatures. The upstream electron temperature may affect the magnetic reconnection dynamics (Petropoulou et al. 2019), but, in general, the thermal plasma in the reconnection upstream is not expected to make a considerable contribution to the blazar emission, as shown in most studies of blazar spectral fitting (Böttcher et al. 2013). Finally, we also study the emission from a larger simulation box, so as to examine whether the results are applicable to larger physical sizes, which are necessary in realistic blazar models.

4.1. Magnetization Factor

We consider two other magnetization factors, $\sigma_e = 10^4$ and $\sigma_e = 1.6 \times 10^5$ (Figure 12). Since we use proton-electron plasma with a real mass ratio, they correspond to $\sigma \sim 5$ and $\sigma \sim 87$, respectively. We normalize the strength of their antiparallel magnetic field components to the same value, $B_0 \sim 0.1$ G at the beginning of the simulation, while the other parameters are kept at their reference values. Comparing these two cases, we find that there is more magnetic energy dissipated with higher magnetization factor (Figures 13 and 14). Also we see more nonthermal particles accelerated in the case MF2. Nevertheless, the overall plasmoid production and mergers appear qualitatively similar between the two cases. Comparing to the study of different guide fields in the previous section, the magnetization factor does not appear to play as important a role in the plasmoid evolution as the guide field strength within the parameter regime that we are interested in here.

Figure 12 shows the light curves and polarization variations for these cases. Since higher magnetization leads to more particle acceleration, the flux level is strongly affected by the magnetization factor. We also notice that the flare peaks later in the run with high magnetization than in the run with low magnetization. The PDs between the three runs are very

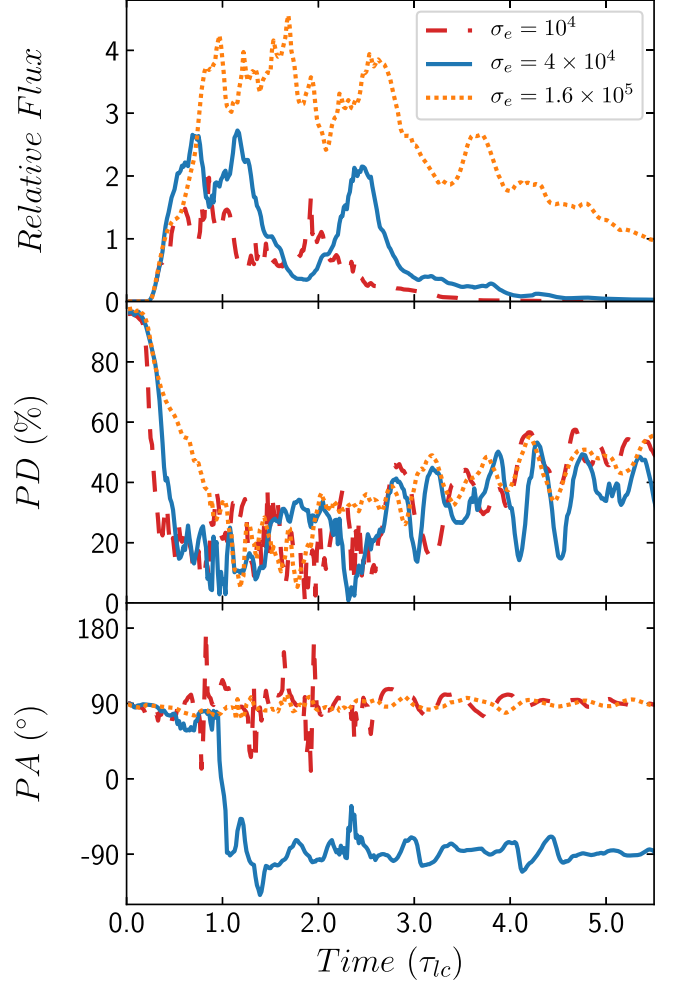


Figure 12. From top to bottom: optical light curves, temporal PD, and PA for different magnetization factors (they are MF1, default run, and MF2). Notice that we rescale the light curves of runs MF1 and MF2 by factors of 5 and 0.5, respectively, to make them appear on the same scale as the default run.

similar, but the case with low magnetization shows strong PA rotations. These behaviors are very similar to those in the default run in different observational bands. Indeed, this is

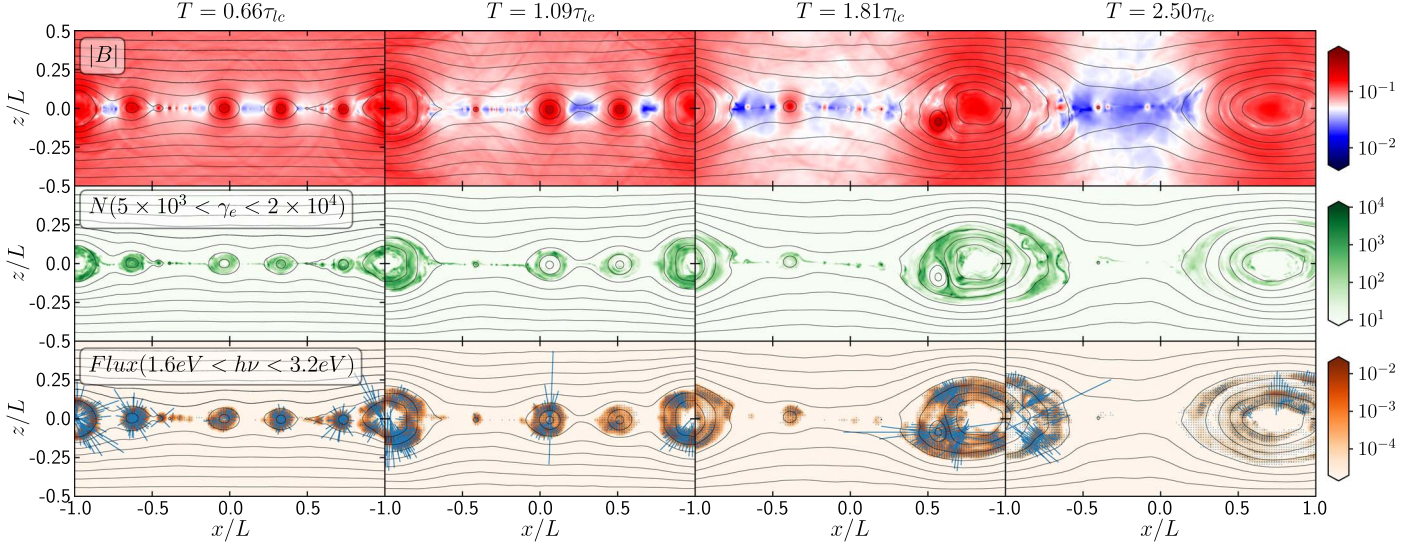


Figure 13. Same as Figure 8 but for the run MF1 ($\sigma_e = 10^4$).

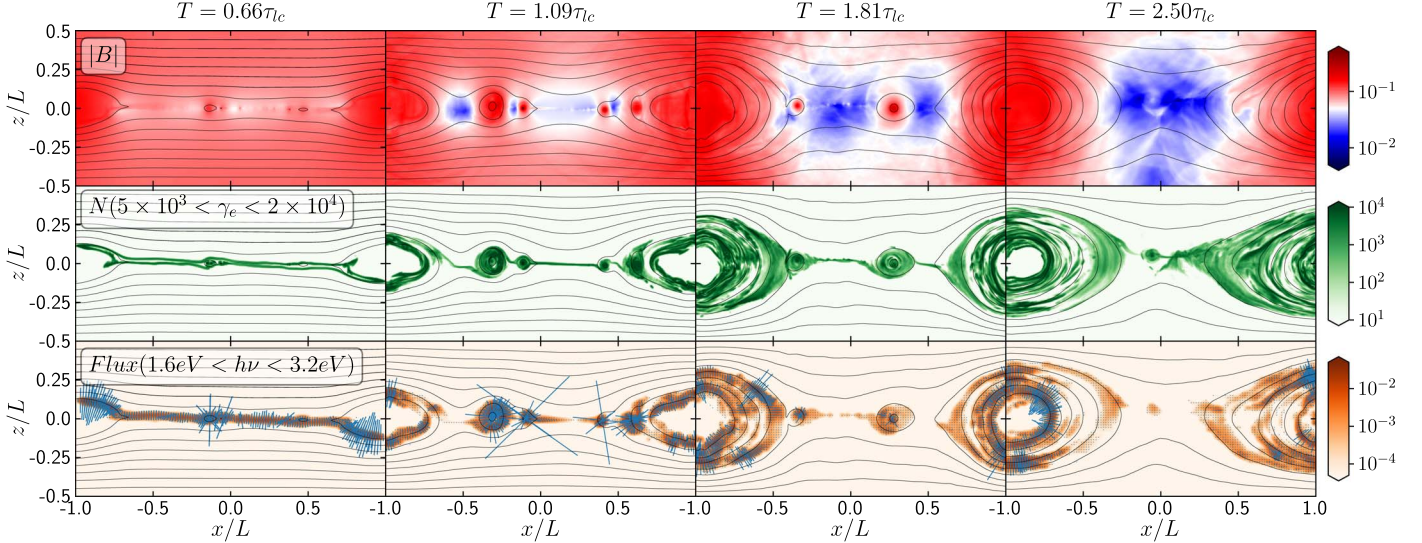


Figure 14. Same as Figure 8 but for the run MF2 ($\sigma = 1.6 \times 10^5$).

because the magnetization factor can affect the spectral shape. It has been shown in previous works that the electron power-law cutoff is approximately at σ_e for magnetic reconnection (e.g., Guo et al. 2014; Sironi & Spitkovsky 2014). Take the case $\sigma_e = 10^4$ as an example: the nonthermal electrons cut off at lower energies than in the default case, so the optical band is around the spectral cutoff, similar to the ultraviolet band in the default case. Therefore, we observe highly variable PD and PA in the optical band for the case with $\sigma_e = 10^4$, similar to the ultraviolet band in the default run (orange curves in Figure 5). Clearly, temporal variations alone cannot diagnose the magnetization factor in the reconnection layer; we need spectral information as well.

4.2. Cooling Factor

The cooling factor C_{10^4} describes how fast the radiative cooling timescale is compared to the acceleration timescale. Since it is a free parameter that we manually add to the simulation, it is crucial to examine how this parameter can

affect the robustness of our results. Figure 15 shows the results. We find that the overall flux level is considerably affected by different cooling factors. This is straightforward to understand, because stronger cooling will reduce the number of nonthermal particles in the reconnection region, leading to lower flux. We also find that the reconnection dynamics and plasmoid evolution are remarkably similar between different cooling factors (Figures 16 and 17), except that the overall evolution is slower for slower cooling. We suggest that the radiative reaction force may play a role in the reconnection dynamics. More importantly, stronger cooling makes the nonthermal particles cool faster, very similar to the different cooling experienced by different observational bands in the default run. The above two effects lead to a delay in the light curves in Figure 15. We observe that the average PD is very similar for different cooling factors, consistent with the different observational bands in the default run. This means that the overall magnetic field morphology and evolution are not affected by the radiative reaction force beyond the evolution rate.

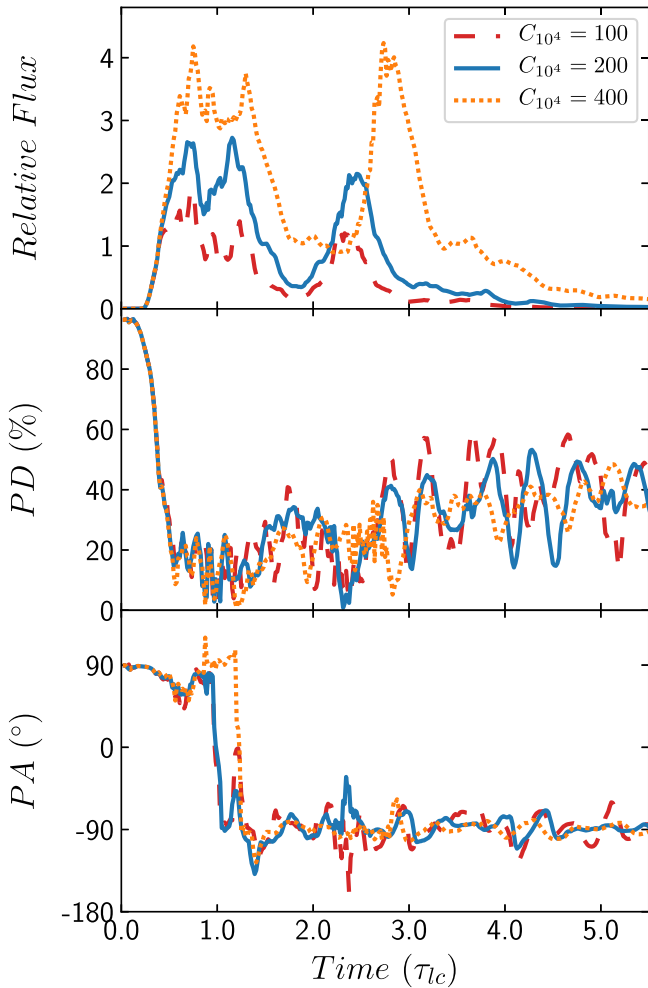


Figure 15. From top to bottom: optical light curves, temporal PD, and PA for different cooling factors (they are CF1, default run, and CF2).

Furthermore, we do not observe any major difference in the PA evolution. The reason turns out to be that the differences between the three cooling factors are relatively small, so that the optical band is at a similar location in the spectrum to that in the default case, i.e., between the cooling break and the spectral cutoff. We also find that there are fewer nonthermal particles for a smaller cooling factor (the run CF1, which means stronger radiative cooling), but the difference is not so large compared to the nonthermal particles that are responsible for different observational bands in the default case (Figure 6). This is understandable, because the cooling factor is only varied by a factor of 2 in our studies. Nonetheless, we have examined that for $2\times$ faster cooling ($C_{10^4} = 50$), the optical PD and PA evolution become very different from the default case, and qualitatively similar to the ultraviolet curve in the default run in Figure 5. Based on the discussion in this section and the previous section on the different observational bands, we conclude that the patterns of polarization variation depend strongly on the position of the observational band on the blazar SED. Specifically, if the observational band is close to the spectral cutoff, the PD and PA can be highly variable; but if it is around or before the cooling break in the SED, the PD and PA generally show small and erratic fluctuations around some average value.

4.3. Upstream Temperature

Since the blazar zone is a highly energetic region, electrons therein may be significantly heated. As suggested by models of blazar spectral fitting, the upstream electron temperature, which is often modeled as the low-energy electron spectral cutoff, can be as high as a hundred to a few thousand m_ec^2 (e.g., Böttcher et al. 2013; Paliya et al. 2018). Additionally, since the PIC simulation needs to resolve the thermal electron inertial length d_e , lower upstream temperature requires higher resolution. Thus for practical reasons we just compare two different upstream electron temperatures, $T_e = 100$ (the default case) and $T_e = 400$ (Figure 18). Apparently, the light curves and PD are very similar in the two cases, except that the case $T_e = 400$ shows higher flux. This is likely because the thermal particles start from higher energies, so that more nonthermal particles are accelerated. In the PA evolution, the case $T_e = 400$ does not show a $\gtrsim 180^\circ$ swing at the second flare, but it does show a PA rotation of $> 90^\circ$ during its last flare. This suggests that the large plasmoid mergers can still dominate the emission in the reconnection layer. As shown in Figure 19 the nonthermal particle evolution and polarized flux appear remarkably similar to those in the default run (Figure 6, third and fourth rows). The lack of $\gtrsim 180^\circ$ PA swing during the second flare is probably because the large plasmoid mergers happen to have symmetric production of nonthermal particles in clockwise and counter-clockwise directions. We notice that Petropoulou et al. (2019) have found that the different upstream temperatures may affect the reconnection dynamics. But their studies have investigated drastically different upstream temperatures. In our parameter study, we only vary the upstream temperature by a factor of 4. Apparently, it only slightly affects the particle acceleration during large plasmoid mergers at the second flare. Therefore, we suggest that the upstream temperature does not play as important a role as other parameters in radiation and polarization signatures from reconnection.

4.4. Box Size

The physical processes that are responsible for the time-dependent radiation signatures, especially the polarization signatures, are the production of plasmoids and secondary reconnection at the plasmoid mergers. As we can see in the simulations, these processes are not subject to the particle kinetic scales that PIC simulations mostly deal with. Nevertheless, it is very important to examine whether these patterns may change with a larger simulation box. We pick a box that is twice as big as the default case in both x and z directions, and redo the simulation with the same parameters as the default run. Figure 20 shows the results. Apparently, all observable signatures, including polarization variations, are very similar to the default case. We remind readers that for both time-dependent signatures and snapshots of the simulation domain we use the light-crossing timescale as the time unit. Now that the simulation box is twice as large, the light-crossing timescale is also twice as large. Therefore, the snapshots in Figure 21 are taken at twice the evolution time of the default case and represent more mature states in the evolution of reconnection. This is also evident from the light curve and polarization variation, where the signatures appear very similar to the default case if we stretch them by a factor of two. Readers may notice that the large box simulation does

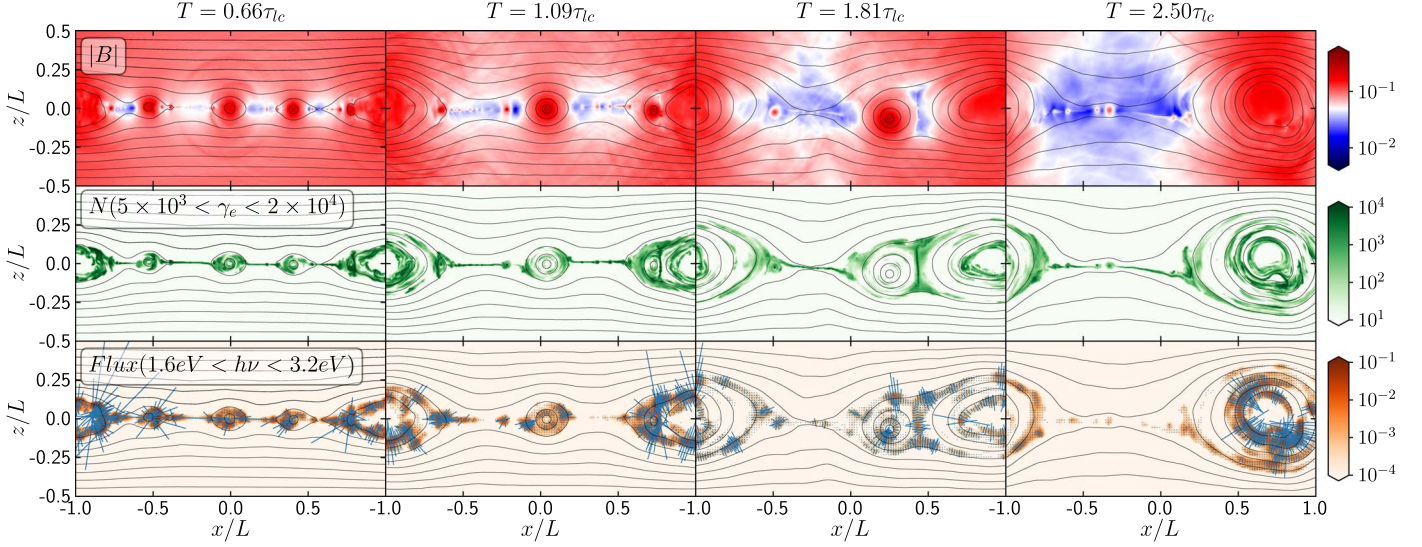


Figure 16. Same as Figure 8 but for the run CF1.

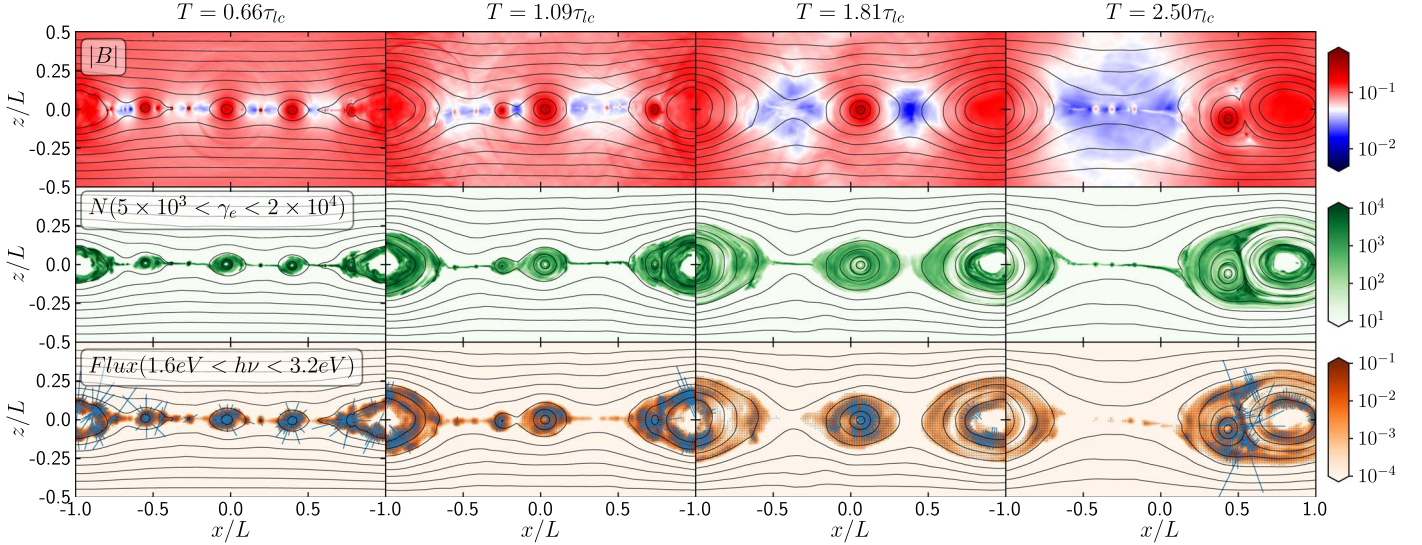


Figure 17. Same as Figure 8 but for the run CF2.

not show a $\gtrsim 180^\circ$ PA swing as in the default case. We remind readers that large PA swings require continuous plasmoid mergers that have asymmetric nonthermal particle acceleration at the secondary reconnection site in the same direction. As mentioned in the default run, the large PA swing is due to two large plasmoid mergers in which both have more nonthermal particle streaming in the clockwise direction. In the large box simulation, however, we find some plasmoid mergers happen to have more particles streaming in the counterclockwise direction. For instance, readers may refer to the third column in Figure 21. There is a large plasmoid merger ongoing at the right end of the simulation box, which has more nonthermal particles streaming counterclockwise, where we find considerable polarized flux in the lower half of the simulation domain. Additionally, we can see in Figure 20 that between τ_{lc} and $2\tau_{lc}$, there are multiple $\sim 90^\circ$ PA swings going up and down, indicating that the direction in which the nonthermal particles are streaming during different large plasmoid mergers keeps changing.

5. Implications for Observations

Relativistic magnetic reconnection can exist widely in magnetized plasma in astrophysical systems. In particular, current theories suggest that relativistic jets are launched with very high magnetic energy, which may dissipate to accelerate particles that radiate along their direction of propagation. Our systematic numerical studies on observable signatures from magnetic reconnection have shown intriguing patterns, especially in the polarization variations. Thanks to the comprehensive multiwavelength coverage and detailed optical polarization monitoring programs, blazar observations have collected a large amount of simultaneous multiwavelength data with optical polarization signatures (e.g., Marscher et al. 2010; Blinov et al. 2015, 2018). Here we discuss several potential observable patterns that can be used to identify and diagnose magnetic reconnection in blazar jets.

We find an overall harder-when-brighter trend from reconnection. In blazar observations, this trend is frequently seen at all wavelengths, including in both the synchrotron

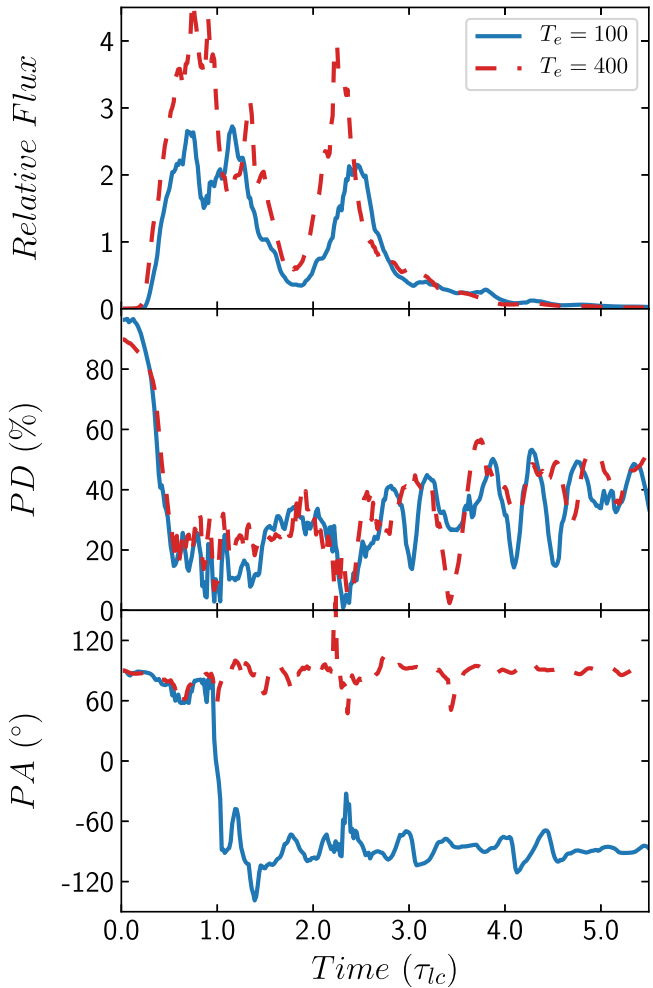


Figure 18. From top to bottom: optical light curves, temporal PD, and PA for different upstream temperatures (they are the default run and UT1).

spectral component and the high-energy spectral component (Giommi et al. 1990; Abdo et al. 2010; Krauß et al. 2016). As shown in Figure 2, the particle spectra show this trend as well. Therefore, we expect that in a leptonic model, where the high-energy component is due to Compton scattering of the same electrons that produce the synchrotron emission, we should expect the same harder-when-brighter trend in X-rays and γ -rays.

Magnetic reconnection exhibits characteristic radiation and polarization trends in multiwavelength observations. These include earlier flare peaks for higher-energy bands in the synchrotron spectral component, and more variable polarization signatures—in particular, large PA swings. Apparently, the difference in polarization signatures between different observational bands depends on the position of the observational band on the blazar SED. The time delay between peaks in higher-energy bands and in lower-energy bands is apparently proportional to the energy difference between the two bands. For FSRQs, this delay may be hard to detect, given that the typical FSRQ spectrum starts to cut off beyond optical bands. However, for high-frequency-peaked BL Lac objects (HBLs), the X-ray band may peak considerably earlier than the optical band. Furthermore, future X-ray polarimeters, such as IXPE, which is scheduled to launch in 2021, may detect X-ray polarization signatures for bright BL Lacs such as Mrk 421 and

Mrk 501. This study finds highly variable X-ray polarization signatures if reconnection drives the flares in HBLs. However, considering the sensitivity of IXPE and other proposed X-ray polarimeters, it is very likely that these instruments have to integrate over longer timescales to obtain one polarization data point. During this time, if the flare is driven by magnetic reconnection, the PA may have rotated considerably. By integrating these photons, those with perpendicular PA can cancel out their polarization signatures. In contrast, previous works suggest that the shock scenario expects higher PD in the X-ray bands because of the more ordered magnetic field structure at the shock front (Tavecchio et al. 2018). Therefore, if X-ray polarimeters detect significantly lower PD in X-ray bands than in optical bands in most blazar flares, this can be strong evidence of magnetic reconnection in blazars.

Based on our results, large optical PA swings are uniquely associated with small guide fields ($B_g/B_0 \lesssim 0.2$). Previous works have suggested that current sheets may form via magnetic instabilities/turbulence in the jet, or between oppositely oriented stripes in the striped jet (Begelman 1998; Giannios & Spruit 2006; Giannios & Uzdensky 2019). The major difference between instabilities/turbulence and striped jets is twofold. First, if kink instabilities happen on the scale of the blazar zone environment (Mizuno et al. 2009; Guan et al. 2014; Barniol Duran et al. 2017), the current sheets formed therein can be smaller than the size of the blazar zone. Therefore, the radiation and polarization signatures that we present in this paper can happen on very short timescales. Interestingly, such microvariability patterns have been reported in observations (e.g., Pasierb et al. 2020). On the other hand, in a striped jet morphology, the magnetic stripes are created at the central engine and propagate along with the jet. Therefore, the blazar zone can be the location of strong dissipation of magnetic energy within the large current sheets formed between stripes (Giannios & Uzdensky 2019). In this situation, we expect that the variability in radiation and polarization signatures should be of days to a few weeks, typical of the duration of blazar flares (Marscher et al. 2010; Angelakis et al. 2016). The second difference is that kink instabilities or turbulence are unlikely to form nearly perfectly antiparallel magnetic field lines, due to their very disordered magnetic topology. Therefore, we do not expect any large ($\gtrsim 90^\circ$) PA rotations from reconnection in kink instabilities or magnetic turbulence. Very interestingly, the blazar microvariability, which may originate from reconnection in magnetic instabilities/turbulence, mostly shows small PA fluctuations (Pasierb et al. 2020). In contrast, in the striped jet scenario, a large region of antiparallel magnetic field lines with small guide fields is probable. Therefore, large PA swings in blazar jets may point to a striped jet model.

Additionally, we find that these PA swings are accompanied by strong flares. Furthermore, the PD generally stays at a low level during PA swings, but can reach higher levels outside swings. Very interestingly, these features have been reported by the RoboPol team, where they find that PA swings are always accompanied by Fermi γ -ray flares, and the PD during PA swings is about 50% of its value in the quiescent state (Blinov et al. 2016b). Indeed, while PA swings have been reported in many observations, they are rather rare and extreme observational phenomena, which imply very lucky situations such that the magnetic field lines are antiparallel in the reconnection event. The RoboPol program has classified

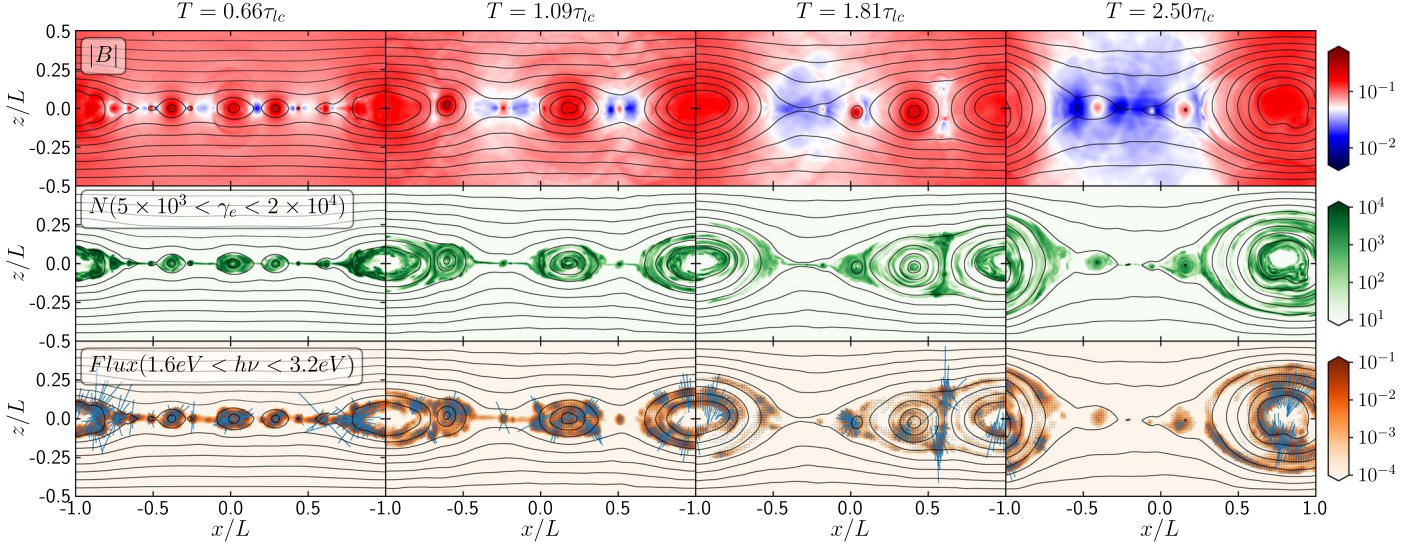


Figure 19. Same as Figure 3 but for the run UT1.

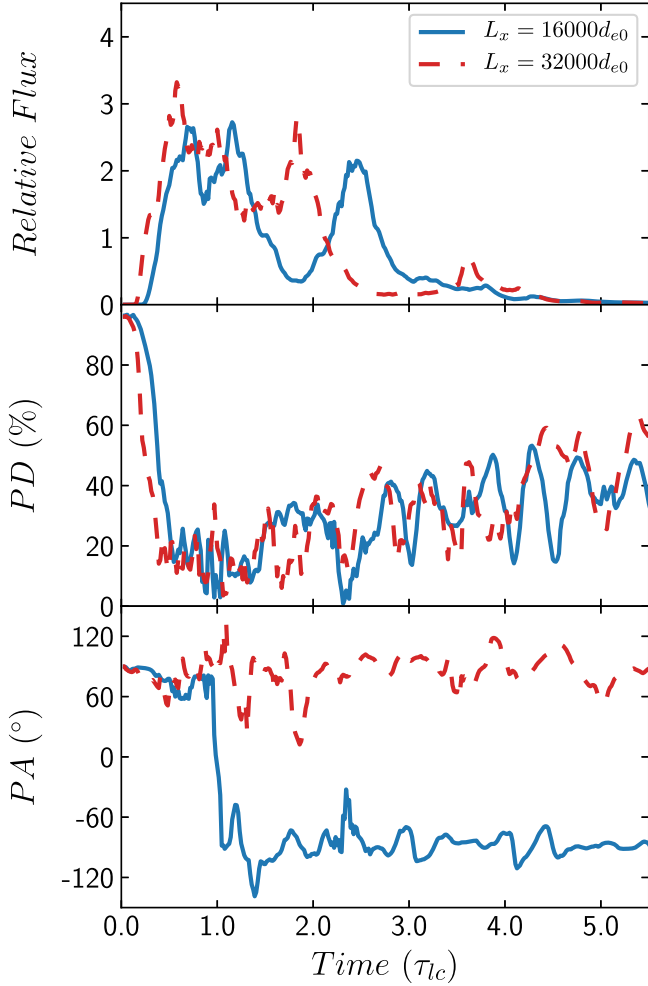


Figure 20. From top to bottom: optical light curves, temporal PD, and PA for different simulation box sizes (they are the default run and BS1). The light curve in the case of the larger box is rescaled by a factor of 0.5 to be in the same figure.

blazars as “rotators” and “non-rotators,” in which the former has shown PA rotations (Blinov et al. 2016a). They have found that rotators appear more active in radiation and polarization

signatures than non-rotators. Based on our simulations, this behavior can occur because rotators are likely striped jets, where reconnection between nearly perfectly antiparallel magnetic field lines is more likely to happen. Consequently, both light curves and polarization signatures appear more variable. We suggest that with better observational statistics, optical polarization signatures can diagnose the physical conditions of magnetic reconnection in jets as well as the overall jet morphology and dynamics.

6. Summary and Discussion

To summarize, we have presented a systematic study of the radiation and polarization signatures arising from magnetic reconnection in an electron-ion plasma in the blazar zone environment. Our studies are based on first principles via PIC simulations, and cover all spectral and temporal radiation and polarization signatures through polarized radiation transfer simulations. Our studies demonstrate that the most crucial physical processes during reconnection that affect radiation and polarization signatures are the production and mergers of plasmoids. In fact, these processes are also unique to magnetic reconnection and do not occur in other blazar flare models that include shocks, kink instabilities, and magnetic turbulence. In particular, we have shown that PA rotations are linked to large plasmoid mergers in the reconnection. Our systematic studies have explored radiation and polarization signatures for different observational bands, guide field strengths, magnetization factors, radiative cooling, upstream temperatures, and simulation box sizes. Based on our results, we have discovered several key observable features in the synchrotron spectral component of blazars from magnetic reconnection:

1. There is a harder-when-brighter trend in the spectral evolution.
2. Observational bands of lower frequencies (infrared to optical) tend to peak later than those of higher frequencies (ultraviolet to X-ray).
3. Lower-frequency bands also show less variable polarization signatures.
4. PA swings are unique to magnetic reconnection with small guide fields ($B_g/B_0 \lesssim 0.2$).

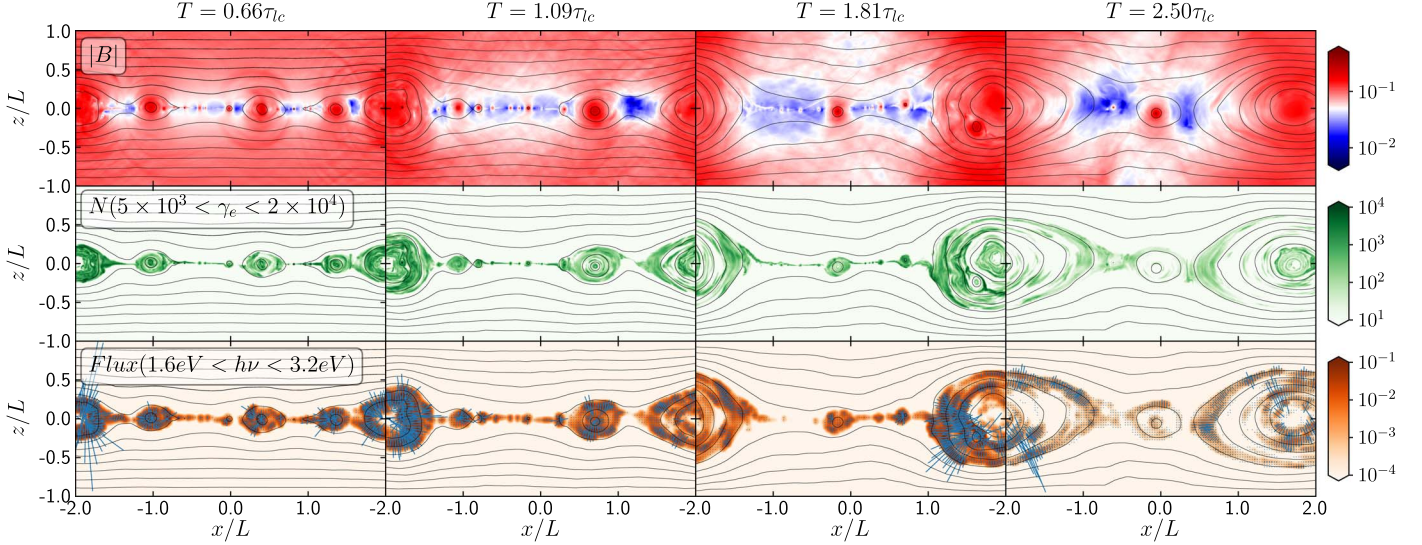


Figure 21. Same as Figure 3 but for the run BS1.

5. PA swings appear simultaneously with flares.
6. The PD generally drops during PA swings.
7. Reconnection with large guide fields ($B_g/B_0 \gtrsim 0.5$) yields low flare levels and very high PD ($\gtrsim 40\%$), which are inconsistent with typical blazar observations.

We have shown that the magnetization factor and radiative cooling play important roles in the spectral shape. Specifically, the difference in the radiation and polarization signatures between different observational bands depends on the location of these bands in the synchrotron spectral component of the blazar. The most important physical parameter in the temporal radiation and polarization signatures is the guide field strength. It is particularly important for polarization signatures. Finally, we have shown that the general radiation and polarization patterns are kept for different simulation box sizes, indicating that our findings may be “scaled up” to realistic physical sizes of the blazar zone environment.

Generally, current sheets can form in magnetic instabilities/turbulence in the jet, or in a striped jet morphology. We expect that the former may result in short-timescale variability in radiation and polarization signatures, because of the highly disordered and dynamical magnetic topology in the instabilities/turbulence, while the latter may lead to strong PA swings and appear very active in both radiation and polarization signatures, since it may give rise to more antiparallel magnetic field lines.

Our studies are based on 2D PIC simulations. Generally speaking, in reality several 3D effects can influence the radiation and polarization signatures. One obvious factor is the viewing angle, which can strongly affect the light-crossing time and the projection of the magnetic field lines that are crucial to both radiation and polarization signatures (Hosking & Sironi 2020). These effects have to be thoroughly studied with 3D PIC simulations. Another issue is that previous 3D PIC simulations have shown that plasmoids in 2D simulations can extend to flux ropes in 3D (Guo et al. 2014, 2015). However, if the guide field is very weak, the 3D flux ropes can quickly fragment into smaller structures, which we expect can lead to similar radiation and polarization signatures as plasmoids (Guo et al. 2020a). On the other hand, if the guide field is strong, it can stabilize the flux ropes. Nonetheless, reconnection is

inefficient with a strong guide field, and we have shown that strong guide fields can result in very high PDs, which are inconsistent with observations. Therefore, we expect that the general radiation and polarization patterns should remain the same in 3D if we are viewing along the direction of the guide field as in our simulations. Finally, 3D reconnection can lead to stronger turbulence. This may lead to even lower average PD than what we find here.

We thank the anonymous referee for very helpful and constructive reviews. This research is supported by Fermi Guest Investigator program Cycle 11, grant number 80NSSC18K1723. H.Z., D.G., and L.D. acknowledge supports from the NASA ATP grant NNX17AG21G and the NSF AST grant AST-1816136. X.L. and F.G. are grateful for support from DOE through the LDRD program at LANL and DoE/OFES support to LANL, and NASA ATP program through grant NNH17AE68I. X.L. and Y.-H.L. are grateful for support from the National Science Foundation grant PHY-1902867 through the NSF/DOE Partnership in Basic Plasma Science and Engineering. Simulations are conducted on LANL’s Institutional Computing machines and Purdue Rosen Center for Advanced Computing (RCAC) clusters. Simulation data can be obtained by emailing H.Z. or D.G.

ORCID iDs

- Haocheng Zhang  <https://orcid.org/0000-0001-9826-1759>
 Xiaocan Li  <https://orcid.org/0000-0001-5278-8029>
 Dimitrios Giannios  <https://orcid.org/0000-0003-1503-2446>
 Fan Guo  <https://orcid.org/0000-0003-4315-3755>
 Yi-Hsin Liu  <https://orcid.org/0000-0001-5880-2645>
 Lingyi Dong  <https://orcid.org/0000-0002-7751-8639>

References

- Aartsen, M. G., Ackermann, M., Adams, J., et al. 2018, *Sci*, 361, eaat1378
 Abdo, A. A., Ackermann, M., Ajello, M., et al. 2010, *ApJ*, 710, 1271
 Ackermann, M., Anantua, R., Asano, K., et al. 2016, *ApJL*, 824, L20
 Aharonian, F., Akhperjanian, A. G., Bazer-Bachi, A. R., et al. 2007, *ApJL*, 664, L71
 Aharonian, F. A. 2000, *NewA*, 5, 377
 Albert, J., Aliu, E., Anderhub, H., et al. 2007, *ApJ*, 669, 862
 Angelakis, E., Hovatta, T., Blinov, D., et al. 2016, *MNRAS*, 463, 3365
 Ball, D., Sironi, L., & Özel, F. 2019, *ApJ*, 884, 57

- Barniol Duran, R., Tchekhovskoy, A., & Giannios, D. 2017, *MNRAS*, **469**, 4957
- Begelman, M. C. 1998, *ApJ*, **493**, 291
- Birn, J., Drake, J. F., Shay, M. A., et al. 2001, *JGR*, **106**, 3715
- Blinov, D., Pavlidou, V., Papadakis, I., et al. 2015, *MNRAS*, **453**, 1669
- Blinov, D., Pavlidou, V., Papadakis, I., et al. 2016a, *MNRAS*, **462**, 1775
- Blinov, D., Pavlidou, V., Papadakis, I., et al. 2018, *MNRAS*, **474**, 1296
- Blinov, D., Pavlidou, V., Papadakis, I. E., et al. 2016b, *MNRAS*, **457**, 2252
- Böttcher, M. 2019, *Galax*, **7**, 20
- Böttcher, M., & Baring, M. G. 2019, *ApJ*, **887**, 133
- Böttcher, M., & Dermer, C. D. 2010, *ApJ*, **711**, 445
- Böttcher, M., Reimer, A., Sweeney, K., & Prakash, A. 2013, *ApJ*, **768**, 54
- Bowers, K. J., Albright, B. J., Yin, L., Bergen, B., & Kwan, T. J. T. 2008, *PhPl*, **15**, 055703
- Cerutti, B., & Beloborodov, A. M. 2017, *SSRv*, **207**, 111
- Cerutti, B., Philippov, A. A., & Spitkovsky, A. 2016, *MNRAS*, **457**, 2401
- Cerutti, B., Werner, G. R., Uzdensky, D. A., & Begelman, M. C. 2012, *ApJL*, **754**, L33
- Cerutti, B., Werner, G. R., Uzdensky, D. A., & Begelman, M. C. 2013, *ApJ*, **770**, 147
- Chandra, S., Zhang, H., Kushwaha, P., et al. 2015, *ApJ*, **809**, 130
- Christie, I. M., Petropoulou, M., Sironi, L., & Giannios, D. 2019, *MNRAS*, **482**, 65
- D'Ammando, F., Raiteri, C. M., Villata, M., et al. 2011, *A&A*, **529**, A145
- Deng, W., Zhang, H., Zhang, B., & Li, H. 2016, *ApJL*, **821**, L12
- Dermer, C. D., Schlickeiser, R., & Mastichiadis, A. 1992, *A&A*, **256**, L27
- Giannios, D. 2013, *MNRAS*, **431**, 355
- Giannios, D., & Spruit, H. C. 2006, *A&A*, **450**, 887
- Giannios, D., & Uzdensky, D. A. 2019, *MNRAS*, **484**, 1378
- Giommi, P., Barr, P., Garilli, B., Maccagni, D., & Pollock, A. M. T. 1990, *ApJ*, **356**, 432
- Guan, X., Li, H., & Li, S. 2014, *ApJ*, **781**, 48
- Guo, F., Li, H., Daughton, W., & Liu, Y.-H. 2014, *PhRvL*, **113**, 155005
- Guo, F., Li, X., Daughton, W., et al. 2019, *ApJL*, **879**, L23
- Guo, F., Li, X., Daughton, W., et al. 2020a, arXiv:2008.02743
- Guo, F., Li, X., Li, H., et al. 2016, *ApJL*, **818**, L9
- Guo, F., Liu, Y.-H., Daughton, W., & Li, H. 2015, *ApJ*, **806**, 167
- Guo, F., Liu, Y.-H., Li, X., et al. 2020b, *PhPl*, **27**, 080501
- Hosking, D. N., & Sironi, L. 2020, *ApJ*, **900**, L23
- Ikejiri, Y., Uemura, M., Sasada, M., et al. 2011, *PASJ*, **63**, 639
- Kiehlmann, S., Blinov, D., Pearson, T. J., & Liodakis, I. 2017, *MNRAS*, **472**, 3589
- Kilian, P., Li, X., Guo, F., & Li, H. 2020, *ApJ*, **899**, 151
- Krauß, F., Wilms, J., Kadler, M., et al. 2016, *A&A*, **591**, A130
- Larionov, V. M., Jorstad, S. G., Marscher, A. P., et al. 2013, *ApJ*, **768**, 40
- Li, X., Guo, F., Li, H., & Birn, J. 2018a, *ApJ*, **855**, 80
- Li, X., Guo, F., Li, H., & Li, S. 2018b, *ApJ*, **866**, 4
- Li, X., Guo, F., Li, H., Stanier, A., & Kilian, P. 2019, *ApJ*, **884**, 118
- Liu, Y.-H., Guo, F., Daughton, W., Li, H., & Hesse, M. 2015, *PhRvL*, **114**, 095002
- Liu, Y.-H., Lin, S.-C., Hesse, M., et al. 2020, *ApJL*, **892**, L13
- Lyubarsky, Y. E. 2005, *MNRAS*, **358**, 113
- Mannheim, K. 1993, *A&A*, **269**, 67
- Maraschi, L., Ghisellini, G., & Celotti, A. 1992, *ApJL*, **397**, L5
- Marscher, A. P., & Gear, W. K. 1985, *ApJ*, **298**, 114
- Marscher, A. P., Jorstad, S. G., D'Arcangelo, F. D., et al. 2008, *Natur*, **452**, 966
- Marscher, A. P., Jorstad, S. G., Larionov, V. M., et al. 2010, *ApJL*, **710**, L126
- McEnerly, J., van der Horst, A., Dominguez, A., et al. 2019, *BAAS*, **51**, 245
- Mizuno, Y., Lyubarsky, Y., Nishikawa, K.-I., & Hardee, P. E. 2009, *ApJ*, **700**, 684
- Morozova, D. A., Larionov, V. M., Troitsky, I. S., et al. 2014, *AJ*, **148**, 42
- Mücke, A., Protheroe, R. J., Engel, R., Rachen, J. P., & Stanev, T. 2003, *APh*, **18**, 593
- Paliya, V. S., Zhang, H., Böttcher, M., et al. 2018, *ApJ*, **863**, 98
- Pasierb, M., Goyal, A., Ostrowski, M., et al. 2020, *MNRAS*, **492**, 1295
- Petropoulou, M., Giannios, D., & Sironi, L. 2016, *MNRAS*, **462**, 3325
- Petropoulou, M., Sironi, L., Spitkovsky, A., & Giannios, D. 2019, *ApJ*, **880**, 37
- Pushkarev, A. B., Gabuzda, D. C., Vetukhnovskaya, Y. N., & Yakimov, V. E. 2005, *MNRAS*, **356**, 859
- Rani, B., Zhang, H., Hunter, S. D., et al. 2019, *BAAS*, **51**, 348
- Rowan, M. E., Sironi, L., & Narayan, R. 2019, *ApJ*, **873**, 2
- Sikora, M., Begelman, M. C., & Rees, M. J. 1994, *ApJ*, **421**, 153
- Sironi, L., Petropoulou, M., & Giannios, D. 2015, *MNRAS*, **450**, 183
- Sironi, L., & Spitkovsky, A. 2014, *ApJL*, **783**, L21
- Smith, P. S., Montiel, E., Rightley, S., et al. 2009, arXiv:0912.3621
- Tavecchio, F., Landoni, M., Sironi, L., & Coppi, P. 2018, *MNRAS*, **480**, 2872
- Werner, G. R., Uzdensky, D. A., Begelman, M. C., Cerutti, B., & Nalewajko, K. 2018, *MNRAS*, **473**, 4840
- Werner, G. R., Uzdensky, D. A., Cerutti, B., Nalewajko, K., & Begelman, M. C. 2016, *ApJL*, **816**, L8
- Yuan, Y., Nalewajko, K., Zrake, J., East, W. E., & Blandford, R. D. 2016, *ApJ*, **828**, 92
- Zhang, H. 2019, *Galax*, **7**, 85
- Zhang, H., & Böttcher, M. 2013, *ApJ*, **774**, 18
- Zhang, H., Chen, X., & Böttcher, M. 2014, *ApJ*, **789**, 66
- Zhang, H., Chen, X., Böttcher, M., Guo, F., & Li, H. 2015, *ApJ*, **804**, 58
- Zhang, H., Fang, K., Li, H., et al. 2019, *ApJ*, **876**, 109
- Zhang, H., Li, X., Guo, F., & Giannios, D. 2018, *ApJL*, **862**, L25